CHALMERS
UNIVERSITY OF TECHNOLOGY

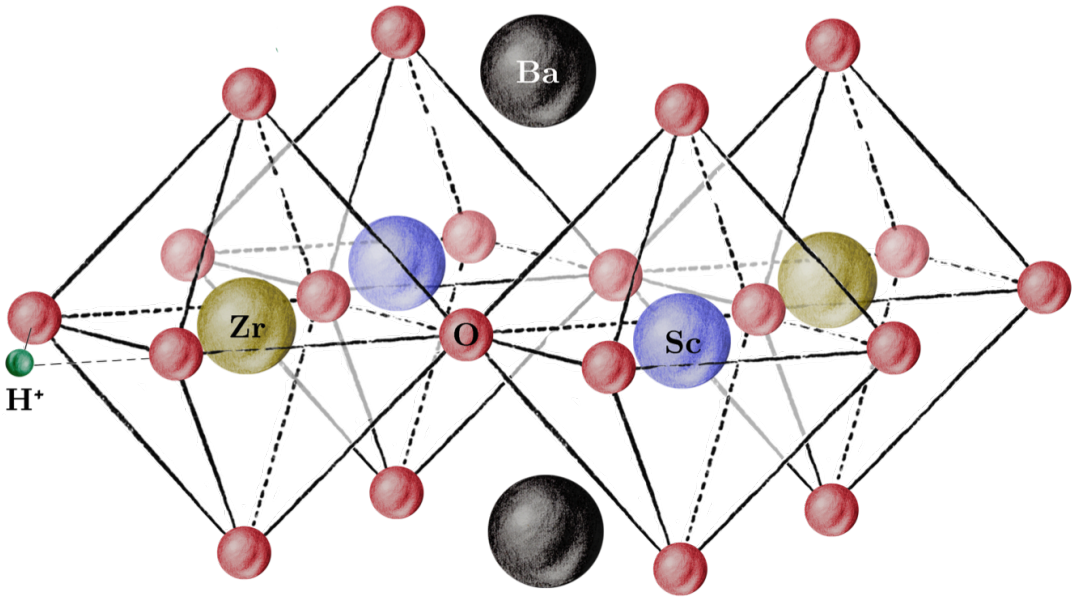

Extending the Momentum Transfer Range in QENS Measurements on Sc-Doped Barium Zirconates

A Study of Local Proton Dynamics

Master's thesis in Applied Physics

JOHANNES ORSTADIUS

Department of Chemistry and Chemical Engineering
CHALMERS UNIVERSITY OF TECHNOLOGY
Gothenburg, Sweden 2019

Master's thesis

Extending the Momentum Transfer Range in QENS Measurements on Sc-Doped Barium Zirconates

A Study of Local Proton Dynamics

JOHANNES ORSTADIUS

CHALMERS
UNIVERSITY OF TECHNOLOGY

Department of Chemistry and Chemical Engineering
Maths Karlsson Group
Chalmers University of Technology
Gothenburg, Sweden 2019

Extending the Momentum Transfer Range in QENS Measurements on Sc-Doped Barium Zirconates
A Study of Local Proton Dynamics
JOHANNES ORSTADIUS

Supervisors: Maths Karlsson, Adrien Perrichon, Carin Österberg; Chemistry and Chemical Engineering
Examiner: Maths Karlsson; Chemistry and Chemical Engineering

Master's Thesis
Department of Chemistry and Chemical Engineering
Maths Karlsson Group
Chalmers University of Technology
SE-412 96 Gothenburg
Telephone +46 31 772 1000

Cover: Structure of barium zirconate where 50% of zirconium cations have been replaced with scandium. A single proton is shown, bonded to its nearest-neighbor oxygen.

Typeset in LaTeX
Printed by Reproservice Chalmers
Gothenburg, Sweden 2019

Extending the Q-range in QENS Experiments on Sc-Doped Proton-Conducting Barium Zirconates
A Study of Local Proton Dynamics
JOHANNES ORSTADIUS
Department of Chemistry and Chemical Engineering
Chalmers University of Technology

Abstract

In this work, a range of scandium-doped, proton-conducting barium zirconates have been subject to two complementary quasi-elastic neutron scattering (QENS) experiments; one featuring a traditional range of momentum transfer (Q) values (0.5 – 2 $Å^{-1}$) and one featuring an extended Q-range (1 – 4 $Å^{-1}$). Recent data suggests that the extended Q-range may allow differentiation between jump and rotational motions of protons within a Grotthuss-type diffusion model. However, so far measurements have been conducted only on the traditional and extended dynamical ranges separately, using different samples. By collecting QENS spectra in both momentum transfer regimes for the same sample, this work aims to achieve a comparison of QENS results over these regimes and their corresponding time-scales. Furthermore, theoretical models for jump and rotational localized motions are compared to experimental data over both Q regimes. It was found that the atomic-scale proton dynamics probed using an extended Q-range are somewhat more rapid (processes with characteristic time-scales of 0.8 – 2.0 picoseconds) than those probed using a traditional Q-range (3.0 – 12.3 picoseconds), as expected from the inherently lower energy-transfer resolution of extended Q-range experiments. QENS measurements further suggested that the more rapid dynamics targeted by the extended Q-range measurement require higher temperatures to initiate. Models for jump-type and rotation-type proton motions both display good fits with the experimental data, preventing discrimination between the models. Nonetheless, it is shown why the extended Q range is useful for ensuring reliability in fitting these models. Activation energies and correlation times are largely consistent with previous measurements on traditional Q-range experiments.

Keywords: proton conductor, Grotthuss mechanism, neutron scattering, QENS, hydrogen bond, barium zirconate, scandium, local proton dynamics

Acknowledgements

To the best imaginable group of researchers and supervisors, for never-ending patience and support: Maths Karlsson, Adrien Perrichon, Carin Österberg, Laura Mazzei, Daria Noferini and Yuan-Chih Lin.
Thank you.
You will find great things.

Johannes Orstadius, Gothenburg, August 2018

Contents

List of Figures

1

Introduction

Proton conduction is an important and widespread process in technology and in nature, both in aqueous and solid media. It occurs spontaneously in water (which happens to be one of the most efficient proton conductors in nature), even more efficiently in ice, as well as in proteins where specific paths have evolved for rapidly transporting protons to reaction centres [1]. However, there are strong indications that protons do not move individually by ordinary translational diffusion – like inert molecules in a gas or liquid would be expected to do when affected by a concentration gradient. Its large (for ions) charge-to-size ratio prevents it from undergoing translational motion by itself without interacting with its surroundings. Neither is the proton transfer process similar to electron transfer; owing to their very small size, electrons may tunnel to any energetically suitable acceptor location within a certain distance (a general maximum around 15 Å can be observed for electron-transfer reactions in organic complexes [2]) even when donor and acceptor locations are not in direct contact. Hence, by virtue of tunnelling, the local structure between a suitable electron donor-acceptor pair is largely irrelevant [2].

Protons on the other hand, being 1800 times heavier than electrons, do not enjoy the same prospects for tunnelling – the likelihood of which varies as $(mass)^{-\frac{1}{2}}$. Plausible tunnelling distances for protons would be shorter than a covalent bond [2]. Instead, proton conduction relies heavily on the local structure around it. This increases the complexity of proton conduction dynamics. Two principal ways for protons to migrate on the atomic scale can nonetheless be distinguished [3]:

1. **Vehicle diffusion**: The proton moves attached to a vehicle such as NH_3 or H_2O (forming NH_4^+ or H_3O^+, respectively). The proton-carrying – hence charged – vehicle may interact with other neutral vehicles in ways that affect the diffusion. If they rather act as non-interacting carriers, this mode of proton transfer can simply be denoted "simple molecular diffusion".

2. **Structural diffusion (Grotthuss mechanism)**: The proton is covalently bound to an atom, but experiences hydrogen bonds (H-bonds) to other oxygen atoms. If one of the H-bonds is strong, the proton can – with relative ease – jump along the H-bond to the next oxygen atom. This is believed to be the principle providing H_2O with prominent proton-conducting abilities. In the case of water, the jump would trigger the new host oxygen atom to release a proton from the opposite side – because it would otherwise be left as an

energetically less favoured H_3O^+ ion. In this way, a sequence of proton jumps occur along a chain of hydrogen bonds. In order to return to their initial state, as can be seen in Fig. 1.1, the water molecules experience a rotational motion after each jump. In other words, the proton transfer is assisted by – on the time scale of the jump – a rigid *structure* of oxygen atoms, providing the origin of the name *structural diffusion.*

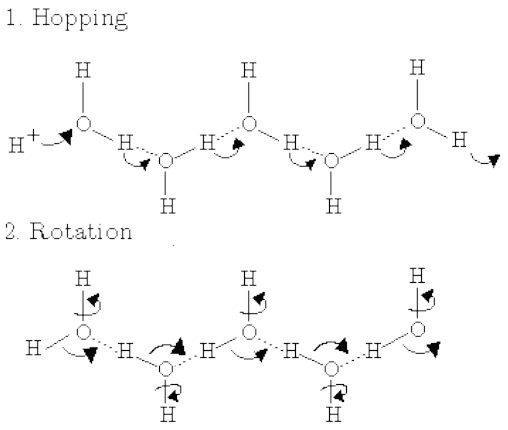

Figure 1.1: The Grotthuss-type proton transfer in a three-molecule segment of water. Figure by Antony Crofts [4].

Already in year 1806, Grotthuss imagined a way that protons could be transported along a chain of water molecules in his work "*Action of Galvanic Electricity upon Certain Bodies Dissolved in Water* [5]". For his time, Grotthuss' principles so well described the phenomenon of structural diffusion of protons through H-bond networks that it is celebrated with his name.

Proton transport in solid matter generally operates by the same Grotthus-type mechanisms as in water [3, 6]. Applied to solid matter, proton transfer can be as useful in technologies as diverse as electrochromics, hydrogen storage and electrolytes in fuel cells converting hydrogen fuel to usable energy [7]. While the basics of how protons interact with the local structure of a solid lattice is rather well understood, but many details necessary to optimize performance of solid proton conductors remains to be clarified. Such details include the variations of proton mobility as a function of structural arrangement of the host crystal, as well as with the chemical composition within each lattice type [6]. Amongst the solid-state proton conductors, materials with the *perovskite* lattice are of particular interest due to their high proton conductivity, good thermal and chemical stability, and high versatility that allows easy control of the properties through chemical composition and doping. The general formula for a perovskite oxide is:

$$A^{2+}B^{4+}{O_3}^{2-}$$

Where O denotes oxygen atom while A and B denotes any cations with oxidation

numbers 2+ and 4+ respectively.

When injected with protons, some materials in this family become some of the most promising options for advancing the high-efficiency solid oxide fuel cell (SOFC) technology. Such fuel cells, oxidizing hydrogen into water and utilizable energy, would be an integral part of a hydrogen-based energy economy. The advantage of SOFC technology is the high efficiency of the cells, however, current fuel cells require temperatures of 600 – 1000 °C to operate [8]. These elevated operating temperatures limit their possible use in mobile applications.

The origin of the temperature restriction is that the electrolyte operates by allowing *oxide ions* to diffuse through the lattice. The temperatures of 600 - 1000 °C are necessary for the oxide ions to become sufficiently mobile. The most widely pursued strategy for lowering these working temperature is replacing the oxide-ion-conducting material with a proton conductor [8]. Diffusing by the Grotthuss-type mechanism, the protons tend to become mobile already in an intermediate temperature range of 200 – 500 degrees Celcius or lower.

However, at the present day, the proton conductors suffer from ionic conductivities too low to make them widely applicable. In order to synthesize solid proton-conductors with improved conductivity, a better understanding of how the protons move on the atomic scale in these perovskite-structured materials is needed.

A particularly promising family of perovskites are barium zirconates (BZO), combining comparatively prominent proton mobility with chemical stability [9]. The protons are introduced into the barium zirconate lattice through acceptor doping. Generally, it is the B-site ions that are substituted with elements of oxidation number 3+ resulting in an overall surplus of negative charge. This is compensated by the formation of oxide-ion vacancies in the lattice. In the presence of water vapour, however, water molecules on the surface breaks down into hydroxide ions (OH^-) and protons, i.e.,

$$H_2O \longrightarrow OH^- + H^+$$

And the hydroxyl (OH^-) ions replace the oxide-ion vacancies in the lattice. The free protons bind to lattice oxygen atom, creating additional hydroxyl ions in the structure. Through this hydration procedure, we have achieved introduction of the hydrogen ions (protons) necessary for proton conduction and once again attained charge neutrality.

The chemical formula of proton-conducting perovskites are hence of the form

$$A^{2+}{B_{(1-x)}}^{4+}{M_x}^{3+}{O_{(3-0.5x+y)}}^{2-} \cdot (H_2O)_{0.5x}$$

Where x is the substitution rate and y is the hydration rate. Common candidate

ions for the A-site are Ba^{2+} and Sr^{2+} whereas Ce^{4+} and Zr^{4+} are common for the B-site [10]. As dopants, ions such as Y^{3+}, Yb^{3+} and Sc^{3+} may be used.

Barium zirconate ($BaZrO_3$, henceforth denoted simply "BZO") with yttrium-doping of x=0.10 ($BaZr_{0.90}Y_{0.10}O_{2.95}$, abbreviated “10Y:BZO”) remains the most widely studied material, displaying higher proton diffusivities than with other dopant ions [11]. Scandium-doped BZO (Sc:BZO), while featuring a proton diffusivity that is two orders of magnitude lower than its yttrium-doped cousin, has been widely studied for the purpose of investigating the microscopic Grotthuss-mechanism in this family of materials. Sc:BZO provides a wide range of achievable doping levels; a doping range of x=0.10 (10Sc:BZO) to x=0.50 (50Sc:BZO) has routinely been synthesized and in 2013, a Tokyo-based group reported synthesis of scandium-doped BZO with x=1.0 (100Sc:BZO), that is, a structure where scandium has fully replaced zirconium [10]. Thus scandium-doped compounds offer an excellent opportunity to study proton dynamics as a function of doping. Proton transfer mechanisms are thought to be very similar for 10Sc:BZO and 10Y:BZO [12], rendering results relevant for the entire family of barium zirconate perovskites.

In Fig. 1.3, the barium zirconate structure is displayed. Note particularly how the protons are bound to oxygen atoms in the lattice, experiencing covalent bonds to their nearest oxygen atoms and hydrogen bonds to their next-nearest oxygen atoms.

The protons move through the oxygen sublattice in a similar way as through the water chain in Fig. 1.1; (i) protons hopping, mediated by hydrogen bonds, between neighboring oxygen atoms and (ii) re-orientational, rotational motion of the hydroxyl group in between such transfers [6]. The second re-orientational step is necessary to prevent the proton from not merely jumping back and fourth between the same two oxygen atoms.

In the doping process, scandium ions replace zirconium ions at the perovskite B-site. Each B-site ion and its six surrounding oxygen atoms are arranged as an octahedron. The choice of B-site ion has a direct impact on the nearby oxygen atoms and protons bonded to them, because zirconium and scandium are different in ionic radius, charge and electronic structure. Hence, the degrees of doping is important not only because it governs the amount of protons but also because it significantly affects the properties of the structure. Therefore, we use different designations separating oxygen atoms neighboring a dopant ion and oxygen atoms not neighboring any dopant ion.

In Fig. 1.2, the jump and re-orientational steps are illustrated for both types of oxygen atom positions.

When we claim to study local proton dynamics, we refer to characterizing the fundamental steps of diffusion; for example which step (hopping or reorientations) is the rate-limiting one and why. What are the time-scales, activation energies and effective distances characteristic for each process? A deeper understanding of how these local diffusion mechanisms are affected by temperature and doping would show the path towards development of new materials with higher proton conductivity.

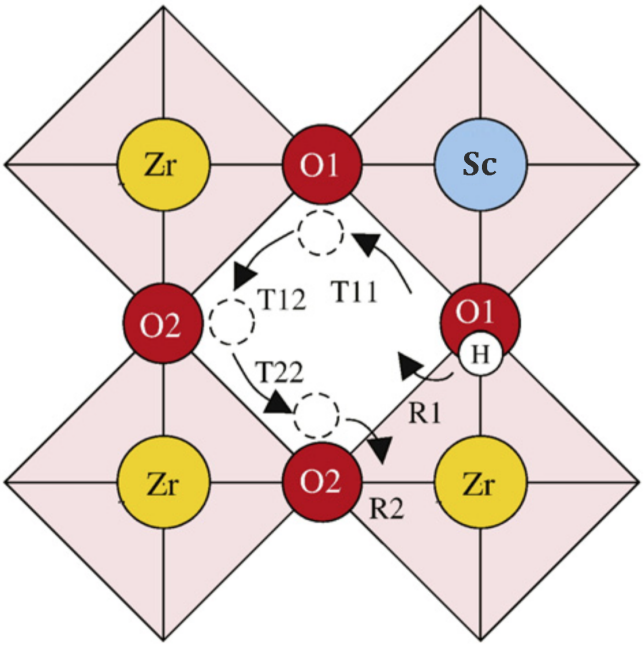

Figure 1.2: Various proton positions and motions in the oxygen atom sublattice of the perovskite. Modified from Ref. [13] with permission.

Lastly, we note that Figs. 1.3 and 1.2 depict the static "0 Kelvin" situation, with cell parameters and bond lengths given as their average values. The figures are disregarding distortions and vibrations, despite the fact that they can make a strong difference for the proton transfers by shortening (strengthen) or lengthening (weaken) the hydrogen bonds.

Given by this background, the aim of the present work is to study local proton dynamics as a function of doping in the full range of scandium acceptor-doping; x=0.10, x=0.50 and x=1.0. This is done through Quasi-Elastic Neutron Scattering (QENS) experiments. QENS is a technique studying diffusion processes on an atomic scale, by detecting the properties of neutrons that have been scattered by *individual* particles undergoing *non-periodic* motion [6]. These particular scattering events result in a unique response; they create a broadening of the elastic peak in a neutron scattering spectra, a broadening which can be observed and analyzed. Because hydrogen ions (protons) exhibit a particularly strong tendency to scatter neutrons, the QENS technique is very well suited to observe diffusion of protons in these materials [12] (cf. Methods). A key element in any scattering experiment is the *transfer of momentum* between scattering centers in the sample, causing scattering, and the moving particles or propagating waves being scattered. In the case of neutron scattering, the momentum transfer (Q) refers to the momentum being exchanged between incident neutrons and particles of the sample (for example protons) during scattering events.

In a recent review [6], one challenge in the field of localized proton dynamics in perovskites was identified to be the lack of experiments conducted under identical

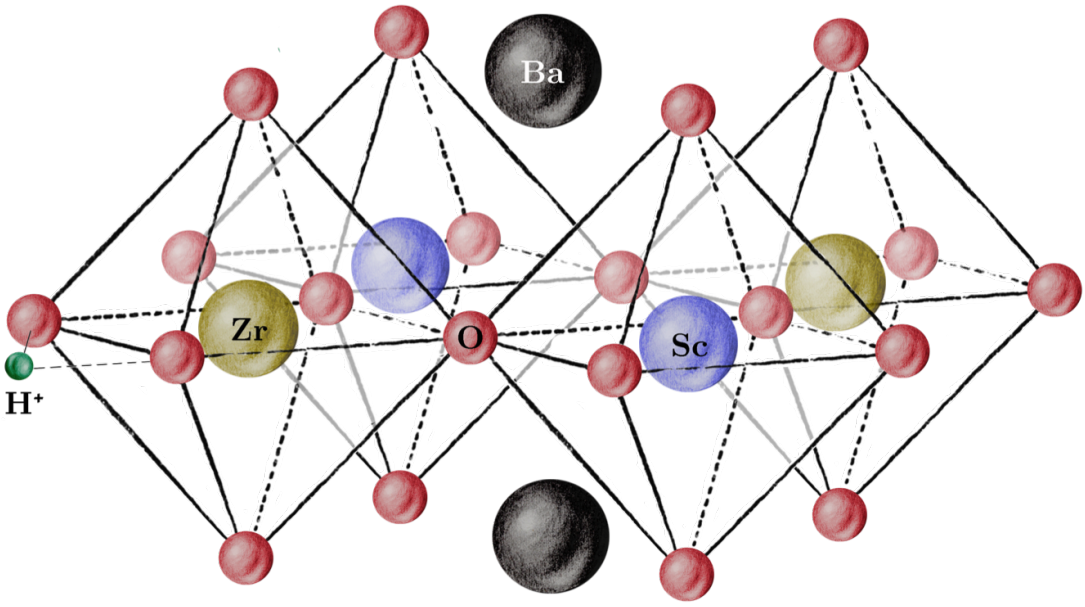

Figure 1.3: A sketch of the 50Sc:BZO perovskite lattice where half of the zirconium ions are substituted by dopant (scandium) ions. A single proton is displayed (left), covalently bonded to its nearest-neighbor oxygen atom and hydrogen-bonded to its next-nearest neighbor.

circumstances and parameters, with well-characterized samples, which has resulted in some reproducibility concerns. Inconsistencies between experimental results are common because of the multitude of instruments used, relatively weak signals, sensitivity to details in data treatments and differences in sample preparation. Hence, in this study, samples with the full range of doping levels have been subject to the same experiment, using identical parameters, allowing a direct comparison of their respective proton dynamics as a function of doping. Another key challenge lays in separating the contributions from jump and re-orientational motions by means of comparing experimental QENS data with theoretical models representing these two types of motions. In particular, the range of momentum transfer (Q-range) used in most studies (roughly 0.2 $Å^{-1}$ <Q <2 $Å^{-1}$) has been considered too limited to aid in the discrimination between models for proton jumps and O-H rotation [13, 6]. For exemple, in Fig. 1.4, taken from Ref. [13], a comparison is displayed between experimental data and models for (i) oxygen-to-oxygen proton transfer and (ii) O-H rotation. Only at momentum transfers as large as 2.5 $Å^{-1}$, the two types of motion appear distinguishable within the particular model and parameters used in the cited study.

To extend the experimental parameters into a range where the responses corresponding to various types of motion are distinguishable, recent experiments [12] covered an extended Q range (1.7 $Å^{-1}$ <Q <4 $Å^{-1}$). Yet, it can be seen from these recent results (Fig. 1.5) that discrimination between jump-type and rotation-type proton motions remain unclear and an accurate comparison between experimental data

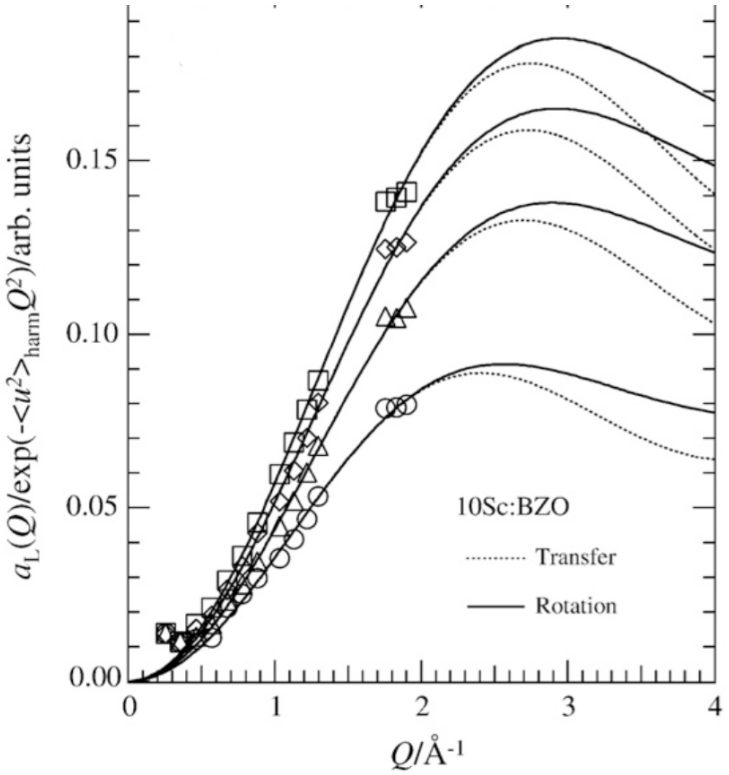

Figure 1.4: A comparison, by Karlsson et al. 2009 ([13]), between experimental data (symbols), a model for proton transfer (dotted lines) and a model for O-H rotation (solid lines). In the cited work, the models are not distinguishable until approximately $Q = 2.5$ Å^{-1}, a momentum transfer range located outside the Q-range of that experiment

.

and models is rendered difficult. Therefore, in the present study, a single 10Sc:BZO sample was investigated in two experiments employing different ranges of Q; one experiment using a significantly extended Q-range (0.57 Å^{-1} <Q <4 Å^{-1}) similar to Ref. [12] and the other employing a traditional, limited Q-range (0.2 Å^{-1} <Q <2 Å^{-1}) similar to Ref. [13]. By virtue of this direct comparison, we elucidate benefits and considerations related to probing the respective ranges of Q.

There is a fundamentally interesting reason to properly characterize the dynamical range related to the extended Q-range: such measurements are related to a lower resolution. A low resolution, as will be discussed in Section 2.1, conceals slow dynamics. Currently, the higher resolution (approx. 70 μeV) provided by limited Q-range measurements tend to probe processes characterized by a time-scale of 10^{-12} to 10^{-10} seconds [14, 6] as seen in Table 1.1. However, some indications suggest the most fundamental motions occur on an even more rapid time-scale. For instance, the H-bond distance may oscillate with a period shorter than a picosecond in case certain photon modes are activated. The lower (approx. 300 μeV) resolution related to extended Q-range measurements are expected to shed light on motions with time-scales *more rapid than* 4 picoseconds (cf. Eq. 2.11), that is, in the low 10^{-12} second range and possibly down into the 10^{-13} second range.

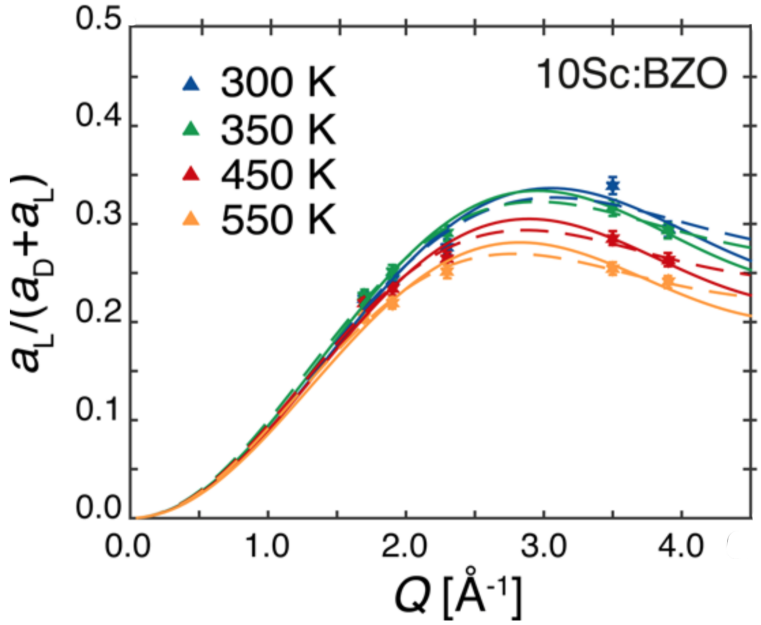

Figure 1.5: Adapted from Ref. [12] (2017), this figure represents recent attempts to refine the model-experiment comparison visible in Fig. 1.4 to an extended range in momentum transfer. It shows that, given the parameters used in Ref. [12], the two local mechanisms are still indistinguishable within the framework of this particular model (cf. Methods)

.

Table 1.1: Time-scales probed by neutron scattering techniques with various energy resolutions. The traditional instrumental parameters used in QENS experiments yield a focus on time-scales in the 10^{-11} second range (tens of picoseconds). Unmodified from Willis [14].

Time scale (sec)	Resolution ΔE (μeV)	Spectroscopic technique
10^{-11}	10 - 100	Direct-geometry time-of-flight
10^{-9}	0.3 - 20	Backscattering crystal analyser
10^{-7}	0.005 - 1.	Spin echo

Lastly, as a control in relation to QENS measurements and previous studies, proton dynamics are investigated also from a H-bond viewpoint *via* vibrational spectroscopy. The O-H stretch and O-H wag vibrational modes visible though these techniques give information on the local environment of the proton, from which depends the diffusion properties.

To sum up, the following efforts are made to elucidate the localized dynamics of proton transfer in perovskites:

- Analysis of QENS spectra as a function of doping in Sc:BZO, using a traditional Q range (0.2 Å^{-1} <Q <2 Å^{-1}).
- QENS analysis of a 10Sc:BZO sample using both the traditional Q range (0.2 Å^{-1} <Q <2 Å^{-1}) and an extended Q range (0.57 Å^{-1} <Q <4 Å^{-1}).

- Fitting of experimental data to models representing hopping and reorientational motions respectively.
- Characterization and control of samples and their proton transfer properties using vibrational spectroscopy, x-ray diffraction and thermogravimetric analysis.

2

Methods

2.1 Quasi-Elastic Neutron Scattering

Neutron scattering provides information about a sample based on the energy and momentum exchanged when neutrons scatters on atomic nuclei in the sample. A scattering event conserves momentum and energy, meaning that any energy or momentum lost(gained) by the neutron has been transferred to(from) the sample. In a scattering situation, the incoming neutron can be represented by a plane wave with wave vector $\mathbf{k}_i$ whose magnitude is related to its energy [14]

$$E_i = \frac{\hbar^2 k_i^2}{2m_n} \tag{2.1}$$

where m_n is the neutron mass, as well as to the incident neutron wavelength

$$\lambda_i = 2\pi k_i^{-1}. \tag{2.2}$$

Because this study deals with powder samples, where crystal orientation on average is random, we are not concerned with the vector nature of the scattering vector $\mathbf{Q} = \mathbf{k}_i - \mathbf{k}_f$ but rather with its magnitude [6]:

$$Q^2 = k_f^2 + k_i^2 - 2k_i k_f cos(2\theta) \tag{2.3}$$

where 2θ is the scattering angle between incident and scattered neutrons.

The transfer of momentum from the neutron to the sample is $\hbar Q$ [15] and the energy exchange in the scattering event is

$$\Delta E = E_i \breve{} E_f. \tag{2.4}$$

A neutron scattering event with positive energy transfer is sometimes referred to as a "Stokes process" and one with negative energy transfer as an "anti-Stokes process", again – from the point of view of the neutron. The number of scattered

neutrons returning with a particular loss(gain) in energy, is monitored as the intensity corresponding to that energy loss(gain). From the *intensity-over-energy transfer* spectrum so obtained, a number of distinct processes can be observed (see Fig. 2.1).

Elastic (i.e. involving no transfer of energy) scattering provides information on atoms *localized* over the time-frame probed by the instrument. Hence, elastically scattered neutrons are the basis of neutron diffraction (ND), used for the study of average structure. When neutrons experience energy exchange with atoms undergoing periodic motion, inelastic peaks arise at energy transfer values corresponding to the frequencies of populated vibrational modes. The study of such peaks is referred to as inelastic neutron scattering. Lastly, non-periodic motions of atoms such as diffusive or re-orientational motion also lead to exchanges of small amounts of energy with the neutron. In contrast to lattice vibrations, there is no energy quantization of these types of motion (on the energy resolution accessible by the instrument) which results in a *continuous* broadening of the elastic peak. The study of this *Quasielastic broadening* can provide valuable information on non-periodic motions such as diffusion processes. The measurements of such non-periodic motions through analyzing broadening of the elastic peak is referred to as QENS. The three types of processes are sketched in Fig. 2.1.

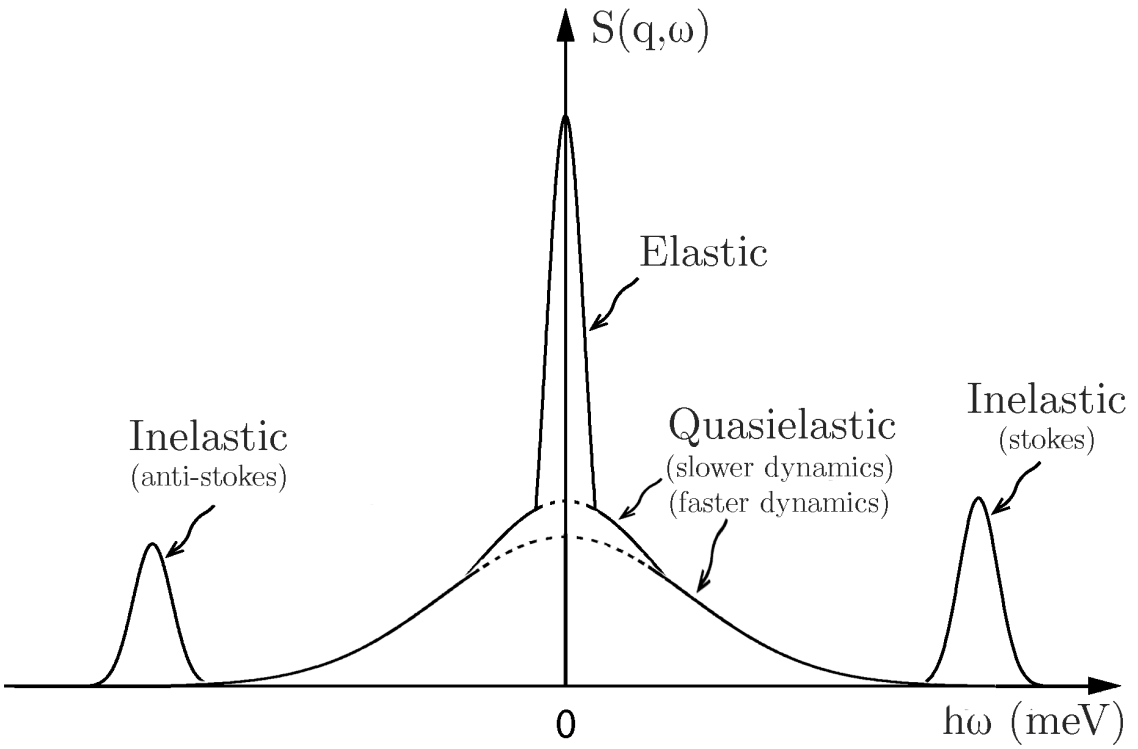

Figure 2.1: Components of the structure factor S(q,ω) in a neutron scattering experiment, showing controbutions from elastic, quasielastic and inelastic scattering. While not obvious from the image, note that the quasielastic contributions feature different widths. The contribution marked "slower dynamics" by definition has a smaller width than the contribution representing processes with "faster dynamics". Figure adapted from [6].

We also need to make a distinction between non-periodic motions related to collective dynamics (where we take into account how the diffusing entities move relative to each other), and non-periodic motions related to the diffusing entities *individually*. The dynamics perceived when observing their movement individually is referred to as self-dynamics. More precisely, we describe the distinction through observing more closely the double differential scattering cross section $d^2\sigma/d\Omega dE$. This quantity, being the basic measured quantity recorded in most neutron scattering experiments, represents the number of neutrons with energy in the range dE scattered into the angular range $d\Omega$, the latter practically representing the angular resolution of the detectors. The probability of scattering depends on the type of atomic nuclei as well as on isotope and spin. Hence, to obtain a *total scattering cross section* characteristic of each element (the scattering probability visualized as a cross section area as perceived by the incident neutron), we need to average over spin and isotopic composition.

Integrating the differential scattering cross section over all energy transfers and the full angular range covered by the detectors, the total scattering cross section can be written as [6]

$$\sigma = \int dE \int d\Omega \frac{d^2\sigma}{d\Omega dE} = 4\pi\langle b^2\rangle \tag{2.5}$$

where b is the *scattering length* and b^2 is proportional to the scattering cross section *area*. In case of b being a complex number, the imaginary part relates to the probability of the atom absorbing the incident neutron rather than scatter it [6]. The total scattering cross section could be expressed as a sum of a *coherent* part σ_{coh} signifying the average over isotopes and spin states of the nucleus

$$\sigma_{coh} = 4\pi\langle b\rangle^2 = 4\pi b_{coh}^2 \tag{2.6}$$

and an *incoherent* part σ_{inc} corresponding to the difference between total and coherent scattering cross sections, i.e. representing the mean-square deviation from average scattering length due to deviations from average nuclear spin or isotopic composition [6]:

$$\sigma_{inc} = 4\pi(\langle b^2\rangle - \langle b\rangle^2) \tag{2.7}$$

We can split the double differential scattering cross section into a sum of contributions owing to coherent and incoherent parts

$$\frac{d^2\sigma}{d\Omega dE} = \frac{k_f}{k_i}\frac{1}{4\pi\hbar}\left[\sigma_{coh}S_{coh}(Q,\omega) + \sigma_{inc}S_{inc}(Q,\omega)\right] \tag{2.8}$$

where the functions storing the Q and ω dependence, $S_{coh}(Q,\omega)$ and $S_{inc}(Q,\omega)$, are analogously called *coherent dynamic structure factor* and *incoherent dynamic*

structure factor, respectively. These functions carry physical information about the sample.

Fourier transforming the dynamic structure factors twice, moving both from the energy to the time domain and from the momentum to real-space domain, we obtain functions referred to as the pair and self correlation functions $G_{pair}(\mathbf{r}, t)$ and $G_{self}(\mathbf{r}, t)$ [15]:

$$S_{coh}(Q, \omega) \xrightarrow{Space\ and\ Time\ FT} G_{pair}(\mathbf{r}, t) \tag{2.9}$$

$$S_{inc}(Q, \omega) \xrightarrow{Space\ and\ Time\ FT} G_{self}(\mathbf{r}, t) \tag{2.10}$$

The physical interpretation of $G_{pair}(\mathbf{r}, t)$ is the probability to observe an arbitrary particle at distance $\mathbf{r}$ after time t relative to the position of a given particle at time $t = 0$, while the interpretation of $G_{self}(\mathbf{r}, t)$ is the probability to observe the *same* particle at distance $\mathbf{r}$ after time t [15].

Hence, the incoherent contribution in a neutron scattering experiment, related to the self-correlation function $G_{self}(\mathbf{r}, t)$ and its Fourier transform counterpart $S_{inc}(Q, \omega)$ are related to the behaviour of *individual* particles in the sample. In QENS, where solely non-periodic motions are probed, coherent scattering can be used to study collective dynamic phenomena e.g. transport properties [**?**], while incoherent scattering probes diffusive or re-orientational motions of individual particles, often referred to as *self-dynamics*. This is what is sought in the present study; accessing information on microscopic proton transfer mechanisms require us to know how protons move individually; proton self-dynamics. Thus only the incoherent scattering from protons is of interest in the present study.

An element may display vastly differing magnitudes for its coherent and incoherent scattering cross sections, governing how prominent the coherent and incoherent scattering will be in relation to each other, and in relation to the coherent and incoherent scattering from other elements. Fortunately, as shown in table 2.1, the incoherent scattering cross section of protons is abnormally large. Noferini [12] estimated the incoherent scattering to comprise a strong majority of the total scattering, and for protons to be responsible for around 96% of incoherent scattering in 10Sc:BZO. This highlights the usefulness of neutron scattering for studies of proton dynamics and ensures that QENS spectra collected in this study are largely owing to from self-dynamics of protons.

In the present study, measurements and discussion concern $S_{coh}(Q, \omega)$ and $S_{inc}(Q, \omega)$, but comparison to their Fourier transform counterparts serves the purpose to clarify some important points: while the experimental results from QENS are formulated in terms of energy and momentum transfer, the information can be translated into time and real-space domains. However, the **time - energy transfer** and **space - momentum** pairs of observables are non-commuting, meaning both quantities in each pair cannot be simultaneously known with perfect certainty. These restrains as

Table 2.1: Cross sections of the elements relevant to this study. Adapted from Noferini [15] with permission.

Element	σ_{scatt} [barn]	σ_{coh} [barn]	σ_{inc} [barn]	σ_{abs} [barn]
H	82.03	1.76	80.27	0.33
O	4.23	4.23	0.0008	0.00019
Zr	6.46	6.44	0.02	0.19
Ba	3.38	3.23	0.15	1.1
Sc	23.6	19.0	4.5	27.5

defined by Heisenberg's uncertainty relations, are applied to our situation by Willis [14]. The energy transfer resolution ΔE of an experiment relates to what time-scales τ are possible to probe [14]:

$$\tau \leq \frac{\hbar}{\Delta E} \tag{2.11}$$

The relation can be intuitively understood from Fig 2.1 by considering that a lower resolution (wide elastic peak) will hide the quasi-elastic broadening corresponding to slower dynamics. The regime of reciprocal space (Q) probed by the experiment is governed by the range in scattering angle and neutron wavelength through the relation [14]

$$Q = \frac{4\pi}{\lambda} sin(\theta) \tag{2.12}$$

for neutrons of wavelength λ elastically scattered through an angle 2θ. Lastly, the dimension in reciprocal (momentum) space Q relates to a length-scale D in real-space simply through

$$D = \frac{2\pi}{Q} \tag{2.13}$$

These three relations (Eq.s 2.11 to 2.13) determine the approximate dynamical range of the experiments as shown in Fig. 2.2.

2.2 Sample Preparation and Characterization

Powder samples of $BaZr_{0.9}Sc_{0.1}O_{2.95}$ (10Sc:BZO) and $BaZr_{0.5}Sc_{0.5}O_{2.75}$ (50Sc:BZO) were prepared (not by this author) using a solid state sintering method by mixing stochiometric amounts of the respective oxides (ZrO_2, ScO_3) and carbonates ($BaCaO_3$), as detailed in Ref. [12]. The powders were hydrated by annealing at 300

°C for several days under nitrogen gas flow saturated with water vapour. As a result, hydrated powder samples $BaZr_{0.9}Sc_{0.1}o_{2.95}(H_2O)_g$ and $BaZr_{0.5}Sc_{0.5}O_{2.75}(H_2O)_h$ were obtained, where g and h should theoretically be equal to 0.05 and 0.25 respectively. Powder of $BaScO_2(OH)$ (denoted 100Sc:BZO for clarity, albeit no Zr content is present) was synthesized in already-hydrated state by Yamaguchi et al, the procedure laid out in detail in Ref. [10]. Key properties of the sol-gel-type synthesis includes a low temperature (300 degrees C) necessary for not dehydrating the sample, and nano-range sizes of the resulting, well-crystallized grains [10]. Thermogravimetric Analysis (TGA) was conducted on all samples in this study, to determine the extent of hydration achieved and indicate whether the protons had been incorporated in the bulk lattice. X-Ray Diffraction measurements were conducted on 100Sc:BZO only, in order to clarify the quantitiative chemical composition of the sample.

2.3 Experimental procedure

For 10Sc:BZO and 100Sc:BZO, QENS measurements were conducted both at the IN6 instrument at Institut Laue-Langevin (ILL) in Grenoble, France and at the TOFTOF instrument at the FRM II neutron source in Munich, Germany. The measurements benefited from complementary of the dynamical ranges probed: the energy transfer resolution difference lead to different time-scales being probed, and the difference in Q range probed by the experiment correlates to different length-scales in direct space. The *dynamical windows* of both experiments are shown in Fig. 2.2 together with instrumental parameters used. For 50Sc:BZO, measurements were conducted solely at IN6.

The powder samples were loaded into flat aluminium cans with sample compartments ranging from 0.5 to 2.0 mm in thickness. Due to high proton concentration, a 0.50 mm thickness was used for 100Sc:BZO while 1.5 mm was employed for 50Sc:BZO and 2.0 mm for 10Sc:BZO. The sample cans were sealed with lead wire to prevent sample dehydration. The same samples and containers were used at both instruments.

The IN6 experiment used a 5.1 Å wavelength resulting in a theoretical 0.21 – 2.08 $Å^{-1}$ momentum transfer range. The TOFTOF experiment employed a 2.5 Å wavelength resulting ideally in a 0.35 to 4.72 $Å^{-1}$ momentum transfer range. Hence, the experiments jointly result in a 0.21 <Q <4.72 $Å^{-1}$ theoretical momentum transfer range corresponding in direct space to a length-scale of 1.33 to 29.90 Å. In reality, the usable momentum transfer is limited by instrumental considerations and Bragg peaks produced by the perovskite host structures, and some ranges (gray regions in Fig. 2.2 were left out. For 10Sc:BZO, QENS spectra were recorded at 19 distinct Q values (9 from IN6, 10 from TOFTOF) from 0.50 $Å^{-1}$ to 4.10 $Å^{-1}$. 50Sc:BZO was only measured at IN6 and thus QENS spectra were recorded at only 9 momentum transfer positions over the range 0.50 to 1.90 $Å^{-1}$. For 100Sc:BZO QENS spectra were recorded at 23 positions in the Q range 0.50 to 4$Å^{-1}$, with 8 spectra from IN6

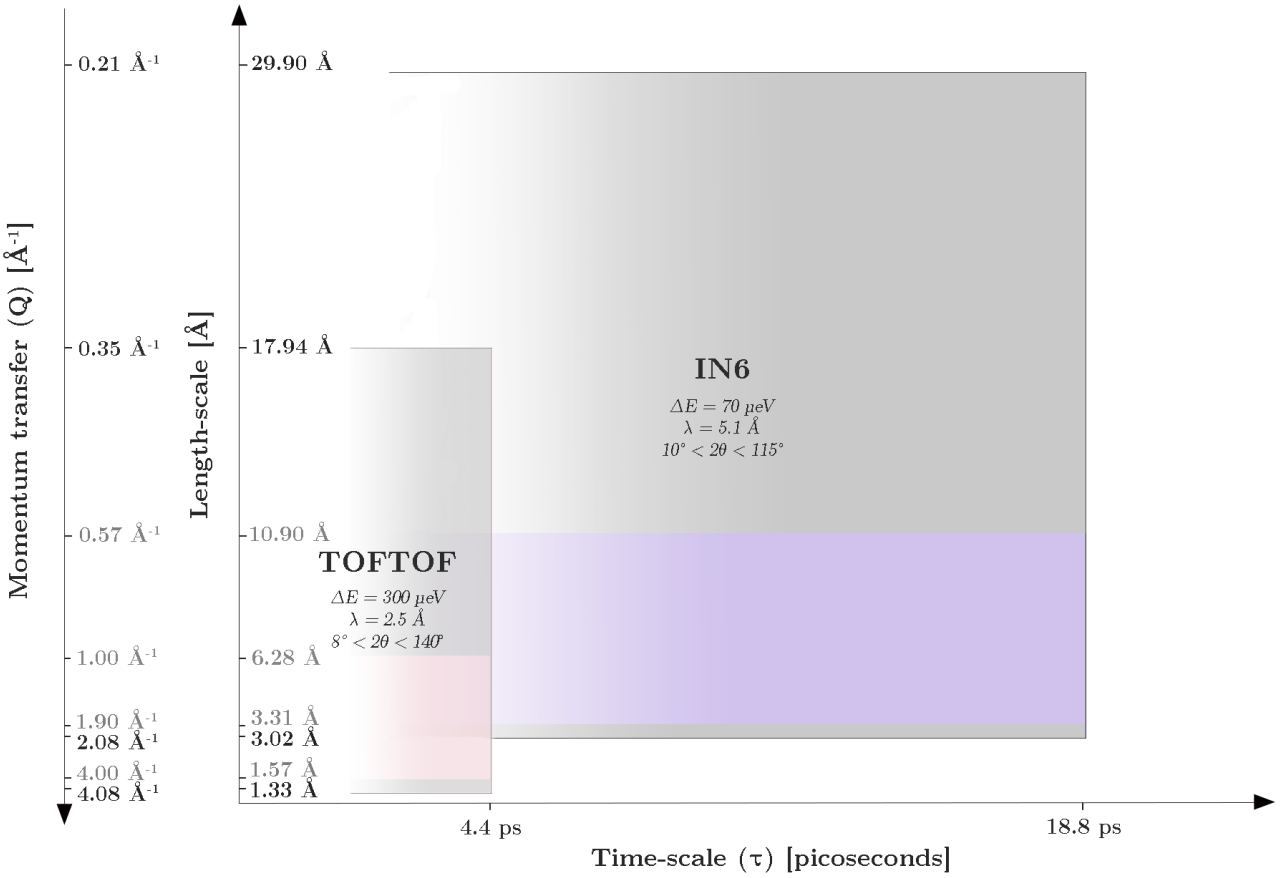

Figure 2.2: Dynamical ranges probed by the experiments. Pink and purple regions refers to dynamical windows containing higher quality data used for the analysis of this work, while the entire areas (including gray) refer to the ideal dynamical range of the instruments. The *dynamical window* rectangles display summaries of instrumental parameters used, where ΔE refers to the full width at half maximum (FWHM) of the elastic peak, λ signifies wavelength of incident neutrons and 2θ is the scattering angle.

and 15 from TOFTOF.

Each spectrum was based on signal integrated over momentum transfer intervals of 0.10 to 0.25 Å $^{-1}$ in width. The QENS spectra recorded for all three structures are summarized in Table 1.

Said wavelengths result in neutron energies of 3.1 meV (IN6) and 13.1 meV (TOFTOF), qualifying incident neutrons as cold (roughly 0.1 – 10 meV) and thermal neutrons (roughly 10 – 100 meV) respectively.

Data was collected for 2 – 4 hours per sample and instrument. Six temperatures in the range 200K to 500K were used at IN6 (200K, 300K, 350K, 400K, 450K and 500K), while 5 temperatures from 300K to 500K (in steps of 50K) were used at TOFTOF. Spectra for the empty sample holder were also recorded at several temperatures in the 300K to 500K range to prevent Bragg peak mismatch due to

Table 2.2: Data points where QENS spectra were extracted for this study. Red text marks data later discarded for quality issues. All values given in $Å^{-1}$.

[$Å^{-1}$]	**10Sc:BZO**		**50Sc:BZO**		**100Sc:BZO**	
	Center	Width	Center	Width	Center	Width
IN6	0.575	0.15	0.575	0.15	0.575	0.15
	0.725	0.15	0.725	0.15	0.725	0.15
	0.875	0.15	0.875	0.15	0.875	0.15
	1.025	0.15	1.025	0.15	1.025	0.15
	1.175	0.15	1.175	0.15	1.375	0.15
	1.315	0.15	1.325	0.15	1.675	0.15
	1.625	0.13	1.675	0.15	1.80	0.10
	1.75	0.15	1.80	0.10	1.90	0.10
	1.875	0.10	1.90	0.10		
TOFTOF	1.10	0.20	No data	No data	1.025	0.15
	1.295	0.19			1.175	0.15
	1.65	0.20			1.325	0.15
	1.825	0.15			1.475	0.15
	1.97	0.14			1.625	0.15
	2.275	0.15			1.775	0.15
	2.82	0.10			1.925	0.15
	3.50	0.18			2.075	0.15
	3.825	0.15			2.225	0.10
	4.00	0.20			2.85	0.20
					3.30	0.20
					3.475	0.15
					3.725	0.15
					3.90	0.20
					4.07	0.14

thermal expansion while subtracting reference.

Data reduction, including suppression of noisy detectors, normalization of detectors using a vanadium reference and transformation from time-of-flight and scattering angle (tof, 2θ) domain to energy and momentum transfer (ω, q) domain, was done within the LAMP software package. Corrections were also applied to the neutron pathlength through the sample due to the slab geometry of sample holder, and to the portion of sample holder subtracted due to absorption of the sample.

Regarding the vibrational spectra collected, infrared spectra were collected on both dry (with hydrogen content removed through heating to elevated temperatures in TGA) and hydrated samples on an IR spectrometer (Bruker Alpha DRIFT) in low pressure. The Raman spectroscopy measurements were conducted using a pump wavelength of 488nm and spectra were collected over a range of 100 to 1000 cm^{-1}. IR spectra were collected from 750 to 5000 cm^{-1}.

2.4 Representation of Experimental Data

The experimentally measured dynamic structure factor $S(Q,\omega)_{meas}$ can be represented by a convolution of a dynamic structure factor $S(Q,\omega)$ with an instrumental resolution function $R(Q,\omega)$:

$$S(Q,\omega)_{meas} \propto S(Q,\omega) \circledast R(Q,\omega) \tag{2.14}$$

The physical information related to proton self-dynamics is contained in $S(Q,\omega)$. To resolve it, the dynamic structure factor $S(Q,\omega)$ was fitted to a simple, three component structure factor composed of a delta function $\delta(\omega)$ representing the elastic peak, one lorentzian function $L(\hbar\omega)$ describing the quasi-elastic broadening and a constant representing a flat background (bkg) according to

$$S(Q,\omega) = a_D(Q)\delta(\omega) + a_L(Q)L(Q,\omega) + bkg \tag{2.15}$$

Combined, we may express the experimentally measured dynamic structure factor as proportional to

$$S(Q,\omega)_{meas} \propto a_D(Q)\delta(\omega) \circledast R(Q,\omega) + a_L(Q)L(Q,\omega) \circledast R(Q,\omega) + bkg \tag{2.16}$$

The model in Eq. 2.16 is fitted to experimental data using the DAVE software, in order to obtain the best-fit weights a_D and a_L i.e. the areas of $D(\hbar\omega)$ and $L(Q,\hbar\omega)$ respectively. These area parameters were extracted and taken to represent each QENS spectrum recorded, as listed in table 2.2, for each temperature. The full width at half maximum (FWHM; henceforth denoted Γ or simply "width") of the lorentzian function $L(Q,\hbar\omega)$ was extracted as a third characteristic parameter related to each QENS spectrum. In Fig. 2.3, the working principle of fitting the structure factor of Eq. 2.16 to the experimental data is displayed. In this figure, spectra for a particular sample, instrument and momentum transfer are displayed for three temperatures. Note particularly how the relative size of the lorentzian function increases with temperature, to account for an increasing quasi-elastic broadening.

The chief objective in the curve-fitting procedure was obtaining a fit true to the overall shape of the elastic peak and quasi-elastic broadening including its “tail”, to correctly capture the width of the lorentzian. The fitting was performed in logarithmic space to more accurately fit the shape of broadening and tail (Fig. 2.3 indeed feature logarithmic scale on y-axes). Due to the scattering intensity values of the tail being very close to zero, the Least Square Error-algorithm employed by the PAN-software in the DAVE package consistently underestimated the width Γ, since

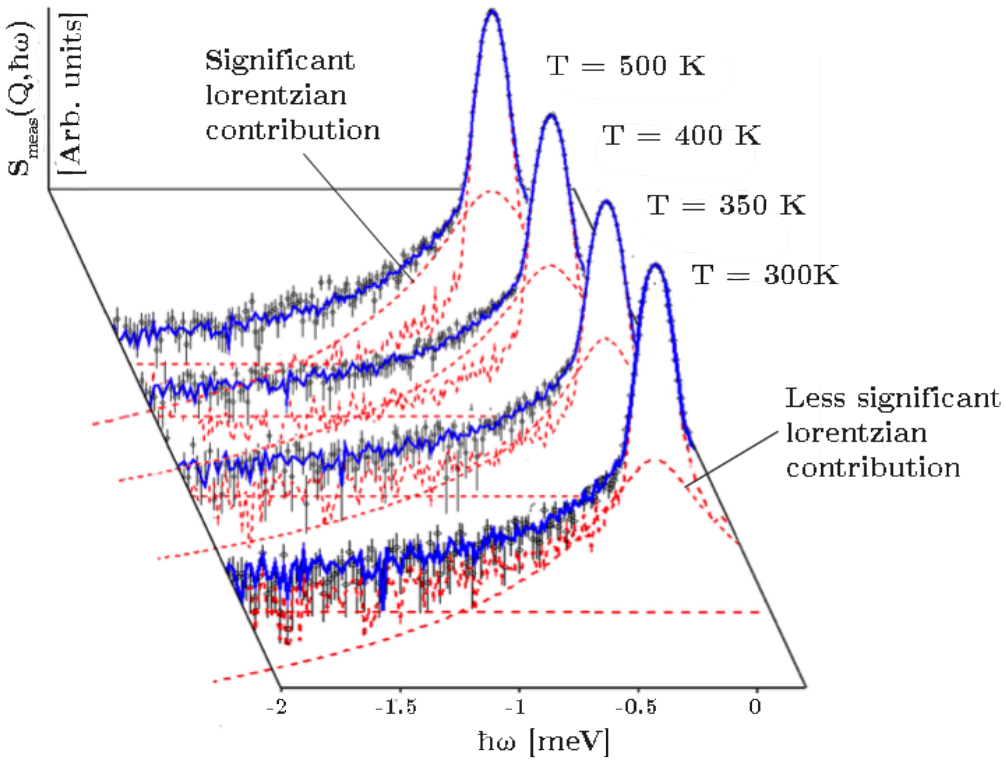

Figure 2.3: Fitting of $S(Q, \hbar\omega)$ from Eq. 1 to IN6 measurements of 10Sc:BZO. Shown here are QENS spectra recorded at $Q = 1.31$ Å^{-1}, displayed at four temperatures. The y-axis is in logarithmic scale. Note how the contribution from the lorentzian function appear to increase with temperatures, representing an increasing quasi-elastic broadening.

minor deviations in the fit for the elastic peak (e.g. due to slight misalignment between resolution function and actual data) were prioritized by the algorithm instead of major deviations of the shape of tail or roots of the elastic peak. For this reason, most data sets had to be adjusted manually to satisfactory fits. See Supplementary Materials (download link on last page) for images of the complete fits for all spectra. In the instances where fitting was adjusted manually, the following procedure was followed:

1. An automatic fit is conducted with components as described above, i.e. one (i) resolution-broadened delta function, (ii) a flat background and (iii) one lorentzian function.

2. The fit of the tail ends is corrected through adjusting the flat background.

3. If a fit is initially loaded from spectra of a nearby temperature, begin by adjusting the area of the lorentzian function. Then determine whether the initial Γ is too large or too small.

4. Identify a reasonable range by trial-and-error by setting Γ obviously too wide

or too narrow, then narrow down a reasonable range.

5. To arrive at best possible fit, attempt various combinations of Γ and lorentzian areas within this reasonable Γ range to obtain a sufficiently good fit of both elastic peak, delta/lorentzian intercept region and tails.

In the instances where fitting was adjusted manually, the PAN software was not able to provide error estimates for the fitting parameters. Instead, errors margins were estimated using the following procedures:

For parameters with distinct dependence on Q (Example: area of lorentzian and delta function components):

- For these parameters a minority of spectra needed manual adjustment. Missing error data was estimated based on the maximum error fraction in available error data for the particular parameter. This method likely resulted in slight to significant overestimation of error margins.

For parameters with no distinct dependence on Q, i.e. parameters possible to describe as distributed around a mean (Example: Γ):

- Standard deviation was calculated from the particular data set. For example, this was viewed the most suitable method for Γ values where no error information was available from measurements for nearby temperatures on the same sample. This method shows a tendency to underestimate error for the first one or two data points, while overestimating the error for all other data points.

- Errors were estimated based on error fractions in related experiment (same settings, environment and sample, conducted at nearby temperature). When information was available from several alternative related meaurements, estimates were based on the highest error values. This method has a tendency to overestimate errors when estimates were based on lower temperature measurements, while underestimating errors when estimates were based on higher temperature measurements.

When fitting IN6 data, the resolution function $R(Q, \hbar\omega)$ was taken to be the 200 K experimental data. This was motivated by previous findings in ref. [12] that the 200 K and 10 K measurements on 10Sc:BZO did not differ measurably in terms of quasi-elastic broadening. For fitting TOFTOF data, no data at lower temperatures than 300 K was available, hence the resolution function was taken as measurements on elemental vanadium of the same geometry; a purely elastic, incoherent scatterer [6].

2.5 Comparison to Models

In order to identify the type of local motions undertaken by the protons, comparisons are made between a model based on known types of motion and experimental results in which types of motion are not known. In previous QENS studies on 10Sc:BZO [12, 13] a jump model was used to differentiate transfer (2-site jump) from O-H rotational motion (thought of as jumps between 4 sites in circular arrangement). The models are based on a dynamic structure factor of the following form [12]

$$S_{jump}(Q,\hbar\omega) = A_0(Q)\delta(\hbar\omega) + \sum_{n=1}^{N} A_l(Q)L_l^{jump}(\hbar\omega) \tag{2.17}$$

for a general number N of equivalent sites arranged in a circle with radius r. Hence, the aforementioned models for transfer and O-H rotation correspond to $N = 2$ and $N = 4$, respectively, in the summation in Eq. 2.17. The model was originally described by Hempelmann in 2000 [16]. In fig. 2.4 we illustrate how the r parameter of the model is assumed to relate to the physical scenarios under study. In fig. 2.4(a) we see how the r parameter in the N=2 model can be taken to correspond to half the jump distance. Similarly, in the $N = 4$ model (fig. 2.4(b)) the r parameter should correspond to a O-H covalent bond length at the time of rotation.

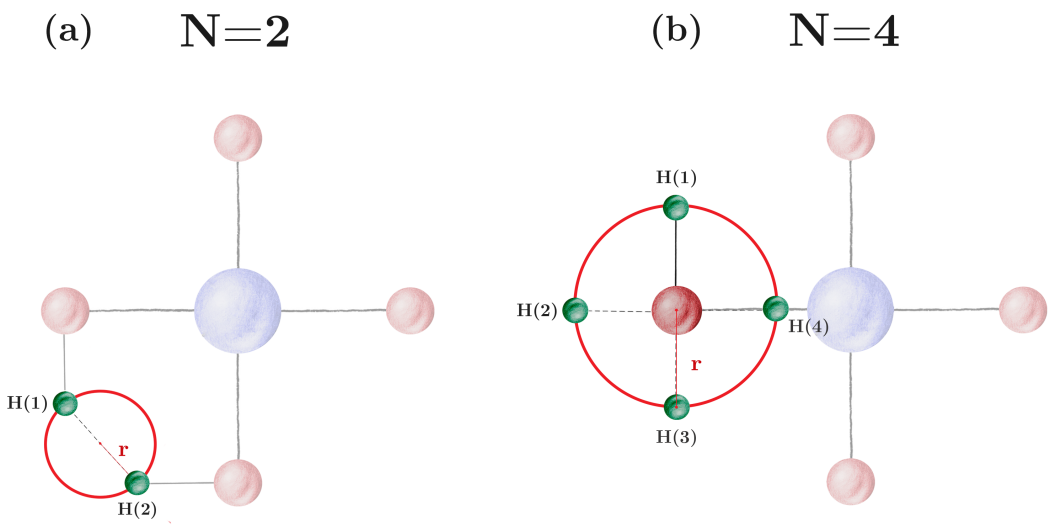

Figure 2.4: Illustration of the $N = 2$ and $N = 4$ models. The r parameters are shown overlaid on sketches of the physical scenarios they are assumed to represent in the context of this study.

The present derivation and expressions are adapted in whole from the supplementary materials of Ref. [12] unless otherwise noted, although the model is also described by Hempelmann [16]. In Eq. 2.17, L is a lorentzian function. The weight A_l of the quasielastic part is given by

$$A_l(Q) = \frac{1}{N}\sum_{n=1}^{N} j_0(Qr_n)cos(\frac{2ln\pi}{N}) \tag{2.18}$$

Here, $j_0 = sin(x)/x$ is the zeroth-order Bessel function, A_l is subject to a normalization condition

$$\sum_{l=0}^{N-1} A_l = 1 \tag{2.19}$$

and r_n are the jump distances under the effect of $(2\pi n/N)$ rotations:

$$r_n = 2r\,sin(\frac{n\pi}{N}) \tag{2.20}$$

To compare experimental results and models, the dynamic structure factor $S(Q, \hbar\omega)$ in Eq. 2.16 representing the experimental data, and the jump model dynamic structure factor $S_{jump}(Q, \hbar\omega)$ in Eq. 2.17, are set equal. Specifically, the point of comparison in this work is the ratio of quasi-elastic scattering intensity to the total scattering intensity (often referred to as Elastic Incoherent Structure Factor (EISF), although this term formally refers to the inverse of this ratio, i.e. the ratio of the *elastic* part of scattering intensity to the total scattering intensity. Both ratios contain the same information). Proton transfer and O-H rotation are related to different signatures in EISF, as can be seen by looking back at Fig. 1.4 and 1.5.

To obtain the EISF expression within the framework of the each model, we (for N=2), set the elastic and quasi-elastic parts equal:

$$a_D(Q)\delta(\hbar\omega) = [A_0(Q) + \epsilon]\delta(\hbar\omega) \tag{2.21}$$

$$a_L(Q)L(\hbar\omega) = A_1(Q)L^{jump}(\hbar\omega) \tag{2.22}$$

to obtain the elastic and quasi-elastic scattering fractions:

$$\frac{a_L(Q)}{a_D(Q) + a_L(Q)} = \frac{A_1(Q)}{1+\epsilon} \tag{2.23}$$

$$\frac{a_D(Q)}{a_D(Q) + a_L(Q)} = \frac{1 - A_1(Q) + \epsilon}{1+\epsilon} \tag{2.24}$$

where, again for N=2, A_1 is calculated according to

$$A_1(Q) = \frac{1}{2}[1 - j_0(2Qr)] \tag{2.25}$$

This procedure requires that the lorentzian function L in Eq. 2.17 can be assumed independent of Q. In the above, the immobile fraction ϵ represents contributions from scattering on atoms moving too slow to be resolved in the quasi-elastic signal of the experiment.

For N=4, setting equal the quasi-elastic and elastic parts respectively for experiment and model, then taking the ratio for each to the total scattering intensity:

$$\frac{a_L(Q)}{a_D(Q) + a_L(Q)} = \frac{A_1(Q) + A_2(Q)}{1 + \epsilon} \tag{2.26}$$

$$\frac{a_D(Q)}{a_D(Q) + a_L(Q)} = \frac{1 - A_1(Q) - A_2(Q) + \epsilon}{1 + \epsilon} \tag{2.27}$$

where for N=4

$$A_1(Q) = \frac{1}{2}[1 - j_0(2Qr)] \tag{2.28}$$

$$A_2(Q) = \frac{1}{4}[1 + j_0(2Qr) - 2j_0(\sqrt{2}Qr)] \tag{2.29}$$

Since only one lorentzian function is used in the representation of experimental data, while for N=4 the model contains two lorentzians, it is necessary to assume a correlation between the lorentzian functions of the model. In this case, the assumption done in Ref. [12] is followed i.e. $\Gamma_2 = 2\Gamma_1$.

EISF of the N=2 and N=4 models is fitted, in order to determine the unknown parameters r and ϵ, to experimental data using a Least Sum of Square Errors algorithm in MATLAB. The best-fit r and ϵ are determined simultaneously, by calculating a matrix with sum of square errors for every combination of r and ϵ, then finding the minimum value of this matrix.

In this work, only the EISF ratios are modelled and presented. Activation energies, mean residence times and other information possible to gain from an analysis of the lorentzian function within the framework of these models have not been calculated.

3

Results and Discussion

3.1 Characterization

The degrees of hydration of the samples was estimated through TGA to be 140 % and 92 % of predicted levels for 10Sc:BZO and 50Sc:BZO, which can be seen from Fig. 3.1). The over-hydration of 10Sc:BZO giving it an actual proton concentration correspoding to 14 % doping, is not extraordinary and does not necessarily imply lack of sample quality in other aspects.

Raman spectroscopy results (shown in Fig. 3.3) and X-Ray Diffraction results (Fig. 3.2) revealed a high fraction of reactant remaining in the 100Sc:BZO sample, which imply synthesis issues or degradation of the sample. Therefore the 100Sc:BZO sample is left out of discussions below.

3.2 Vibrational Spectra

For the hydrated 100Sc:BZO, as pointed out above, we note similarity with several peaks representing reactants in the sol-gel-type synthesis of Ref. [10]. The relevant peaks are marked in Fig. 3.3.

Leaving 100Sc:BZO aside, we compare the Raman spectra of 10Sc:BZO and 50Sc:BZO in Fig. 3.3 to those of previous studies in Fig. 3.4. We first note that the undoped structure (see two Raman measurements of undoped BZO in Fig. 3.4a and Fig. 3.4c) has, on average, a cubic symmetry based on XRD data e.g. in Ref. [17]. As such, it is not expected to show any Raman-active vibrational modes [11]. This can be illustrated by the Raman spectrum of $SrTiO_3$ in the very bottom of Fig. 3.4a, a cubic material that indeed displays an absense of distinct Raman signatures. Hence, the sharp features visible in the Raman spectra of undoped BZO indicate local distortions causing a breakdown of the short-range cubic symmetry.

Previous studies on Y-doped [17] and In-doped BZO [19] suggest that doping increase the prominence of local distortions; Karlsson et al [19] who studied short-range structure over a very wide range of indium doping ($x = 0 - 0.75$) observed strengthening of vibrational modes and emergence of several new ones with increasing doping.

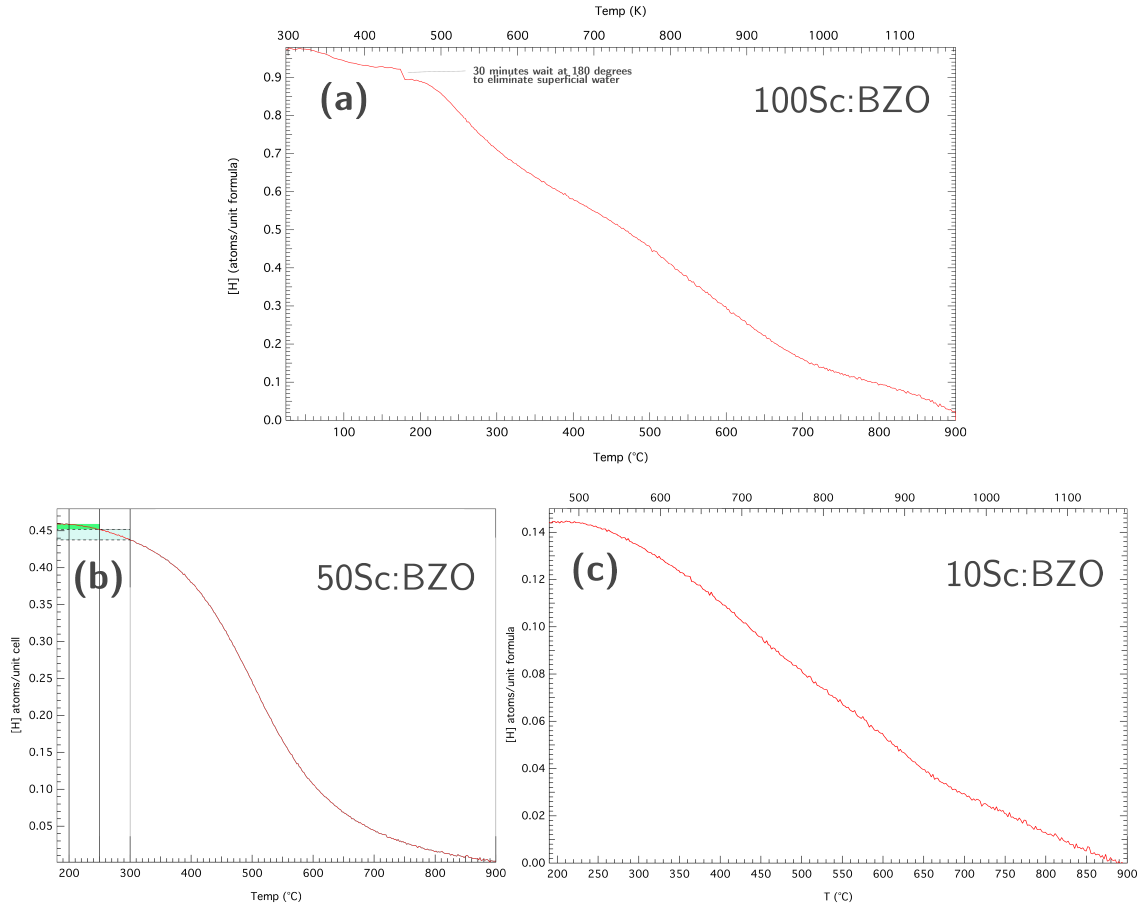

Figure 3.1: Thermogravimetric analysis (TGA) results for the samples. Measurements conducted by Laura Mazzei.

The Raman spectra obtained from our 10Sc:BZO and 50Sc:BZO samples suggest a similar trend, based on the emergence of several modes in 50Sc:BZO particularly in the 200 – 500 cm^{-1} frequency range.

From the comparison between dry and hydrated states of each sample in Fig 3.3, it is clear that the primary differences between undoped BZO and the doped structures are not a result of the introduction of protons (hydration) but rather a result of the substitution of Zr cations at the B-sites. This can be rationalized, at least in part, through the difference in ionic radius between Zr and the dopants (Zr = 0.72 Å, Y = 0.90 Å, In = 0.80 Å, Sc = 0.75 Å [11])

Indeed, previous studies agree that the protons themselves have little effect on the vibrational spectra of barium zirconates. [11, 17, 19]. The hydration rather appears to cause a quenching effect on the Raman-active modes; several vibrational modes are damped or quenched in the hydrated states of 50Sc:BZO relative to its dry state. One vibrational mode at 250 cm^{-1} and one double feature at 400 - 450 cm^{-1} are removed by the hydration.

It has been suggested, based on NRM spectroscopy [20], that 80% of protonic defects

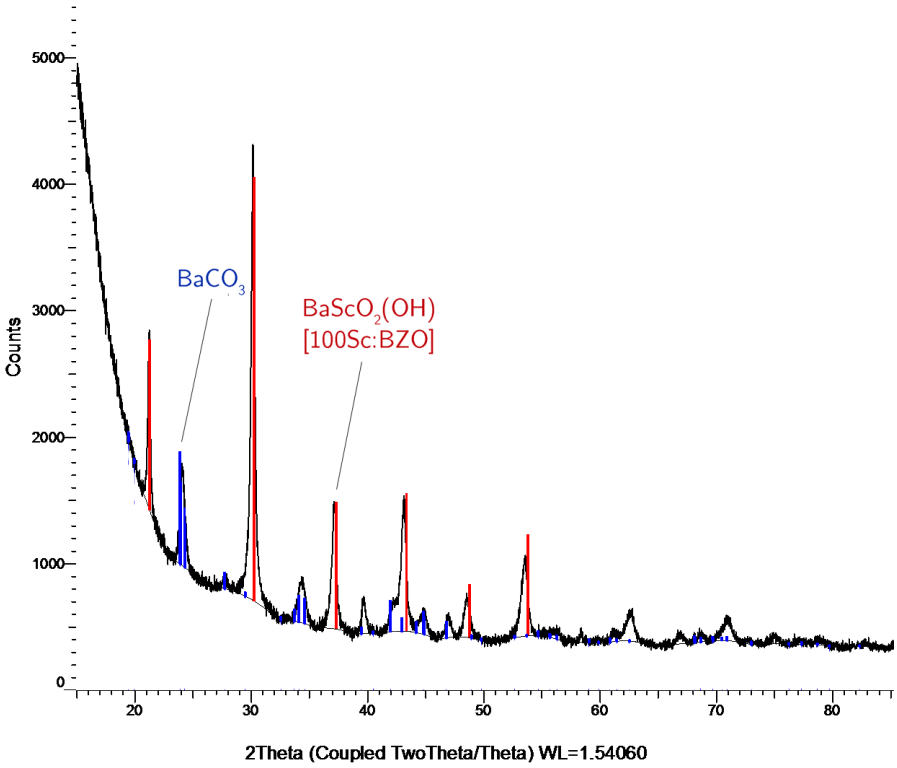

Figure 3.2: X-Ray Diffraction measurement on the 100Sc:BZO sample revealed substantial contamination of $BaCO_3$, a reactant in the synthesis of 100Sc:BZO.

gather around the Sc dopant ions at 10% scandium doping. It would be a plausible consequence that the vibrational modes most significantly affected by hydration would generally be those involving scandium cations.

An assignation of spectral regimes to structural units can be attempted by first-principles calculations. This has been done for Sc:BZO ($x = 0.125$) eg. by Sahraoui *et al.* [18] and their assignation is displayed in Fig. 3.3. In summary, the 100 - 900 cm^{-1} frequency range covers vibrational modes related to the host lattice, with no vibrations directly involving protons [11, 18]. The trends of the simplified harmonic oscillator model, where frequency increases with decreasing mass of the components oscillating, suggests that oscillations directly involving protons would take place with higher frequency. Indeed, we find two modes characteristic of proton content around 1450 cm^{-1} and as wide feature stretching from roughly 2500 to 3650 cm^{-1}); the 1450 cm^{-1} peak corresponds to O-H wag and the 2500-3650 cm^{-1} feature is related to the O-H stretch mode [21, 11, 18].

In analogy, the vibrational modes involving heavy components such as $Zr(Sc)O_6$ octaedra and barium cations, are related to the lowest-frequency features [18]. Most of the vibrational modes emerging with increasing doping reside in this lower frequency region:

- The 138 cm^{-1} peak emerging with Y-doping (Fig. 3.4a) also emerges with Sc-doping.

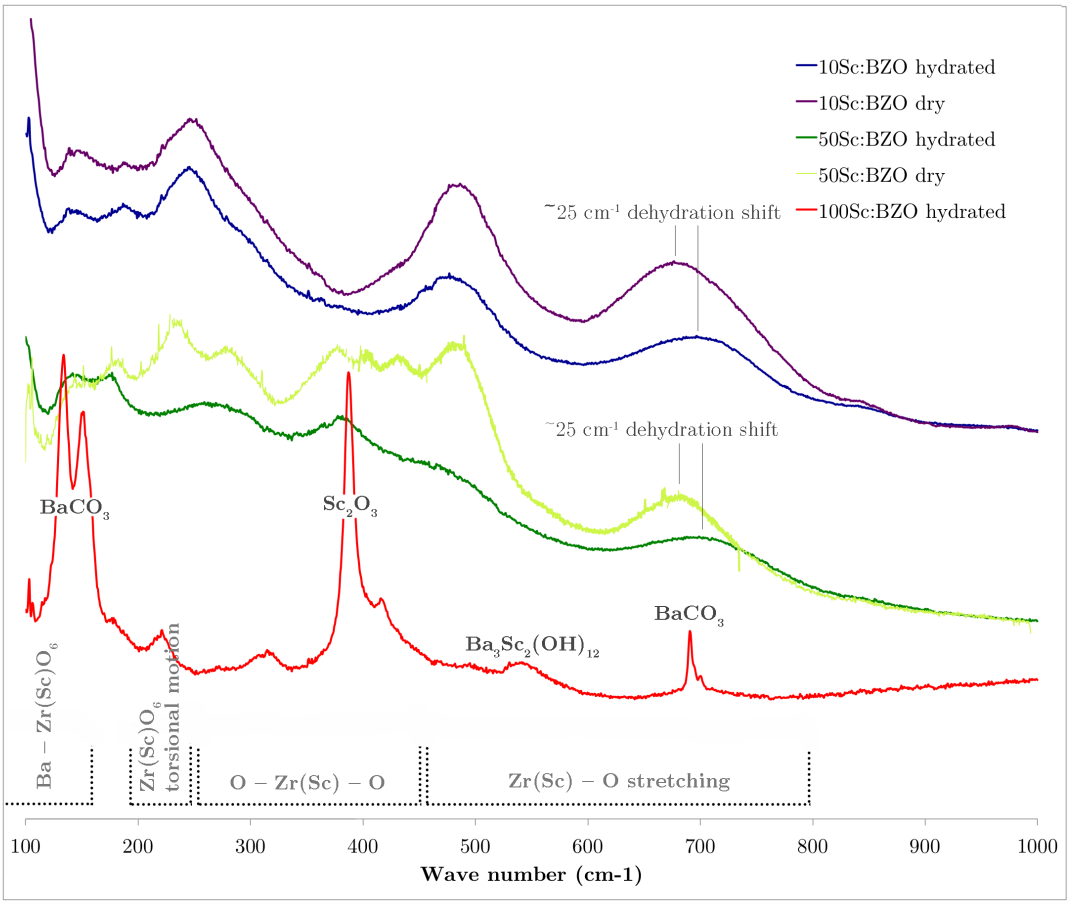

Figure 3.3: Raman spectra of Sc:BZO with $x = 0.10$, 0.50 and 1.0. Approximate assignation to structural units displayed in the bottom, adapted from Ref. [18].

- The 185 cm^{-1} feature visible in undoped BZO and appearing to fade with Y-doping (Fig. 3.4a) appears to remain distinct through the entire Sc-doping regime.

- In undoped BZO, there is a strong feature at 280 cm^{-1}. Giannici [17] suggests this is intensified and frequency-shifted towards lower frequency (230 cm^{-1}) with Y-doping. In 10Sc:BZO and 50Sc:BZO, both the 230 cm^{-1} and the original 280 cm^{-1} peak are simultaneously visible. In 50Sc:BZO, they are comparable in magnitude while for 10Sc:BZO, the original 280 cm^{-1} peak is visible only as a shoulder.

- Four peaks emerging in the 380 - 500 cm^{-1} range in 50Sc:BZO, out of which only the peak near-500 cm^{-1} is readily seen in 10Sc:BZO.

suggesting that doping cause distortions related to the heavy $Zr(Sc)O_6$ octaedral units, where dopants are localized. It is widely believed [11, 19, 17] that an underlying cause for emergence of these spectral features is increasing tilt of these $Zr(Sc)O_6$ octaedra, lowering symmetry enough for otherwise Raman-forbidden vibrational transitions to become Raman-active. The tilt could strongly affect proton

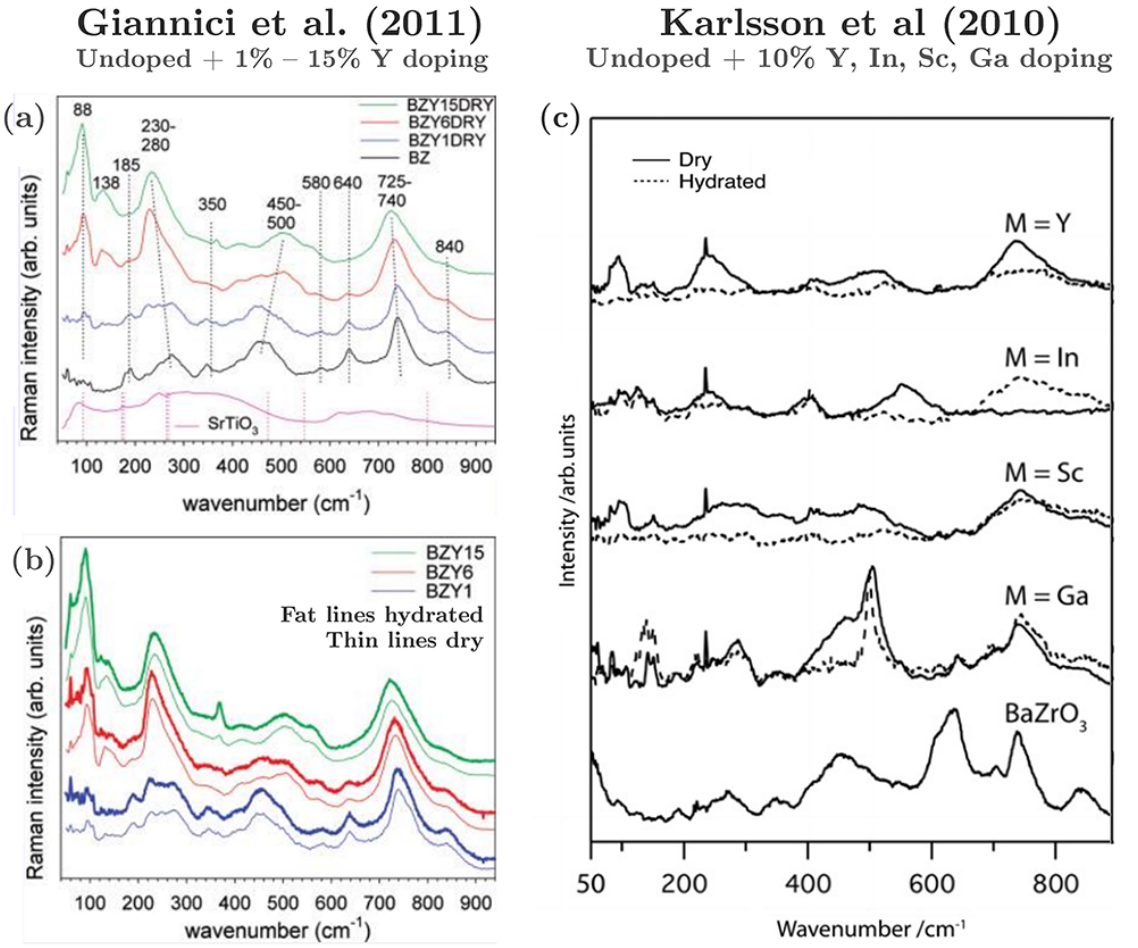

Figure 3.4: Raman spectra of undoped and doped BZO from previous studies. Subfigures (a) and (b) displays Raman spectra of Y:BZO as a function of doping, from Giannici et al 2011 (Ref. [17]). Subfigure (c) shows a comparison between dopants (x=0.10) including Scandium, from Karlsson et al 2010 (Ref. [11]). Subfigures (a) and (c) includes Raman spectrum for undoped BZO from the respective authors.

conductivity, because O-O distances are altered.

Worth mentioning is that the decrease in frequency of the 740 cm^{-1} peak with increase in doping, identified with Y-doping in Ref. [17] and extensively discussed by the authors, is not found with Sc-doping for the corresponding peak (around 700 cm^{-1}). Instead, for Sc-doping, this peak is the only feature consistently frequency-shifted by hydration.

In the infrared (IR) spectra, covering higher frequencies, we can see the aforementioned O-H signatures. Here, doping in contrast appear to *increase* the strength of both features. The broad character of the stretch-related feature is explained by variations in hydrogen-bond strength between the proton and next-nearest oxygen atom. These variations are themselves dependent on possible variations in local envi-

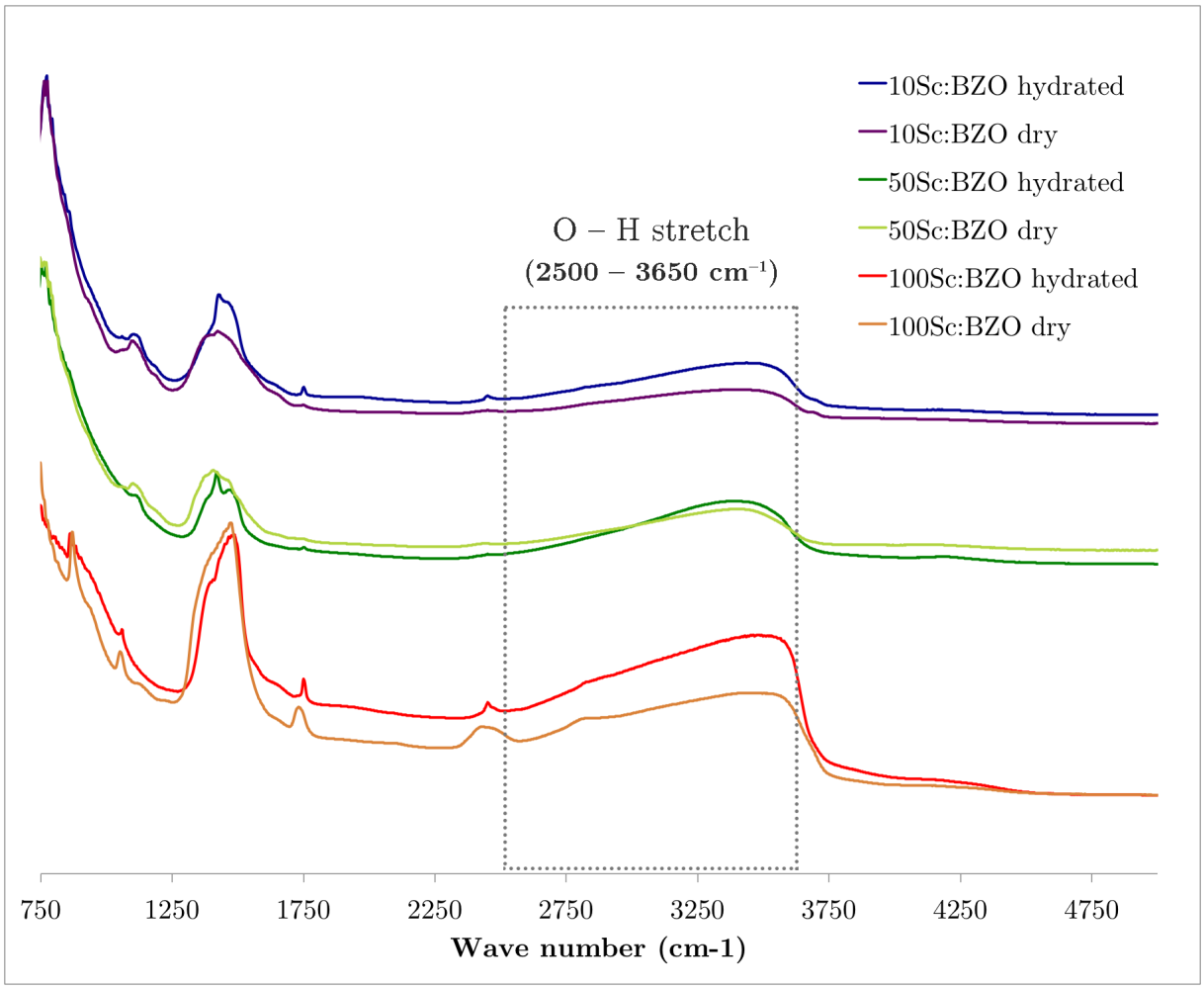

Figure 3.5: Infrared spectra.

ronments, e.g. distance to dopant ion(s), existence of nearby oxygen atom vacancies or other protons and degrees of lattice distortions such as tilting of the $Zr(Sc)O_6$ octahedra.

3.3 Quasi-Elastic Neutron Scattering

3.3.1 EISF analysis

As previously discussed in *Methods*, the EISF relates to the amount of elastically scattered neutrons to the inelastically (in our case limited to the quasi-elastically) scattered neutrons. Hence, it provides a relative estimate of the magnitude of proton dynamics, within the time and length-scale window probed by the respective experiment.

We remind the reader that although the EISF is originally named from the ratio

instead being taken as the *elastic* component to the total scattering, we present the quasi-elastic fraction (causing no loss of information) for clarity:

$$\frac{a_L(Q,T)}{a_L(Q,T)+a_D(Q,T)} \tag{3.1}$$

i.e. the ratio of the quasi-elastic component of scattering intensity to the total (sum of elastic and quasi-elastic) scattering intensity.

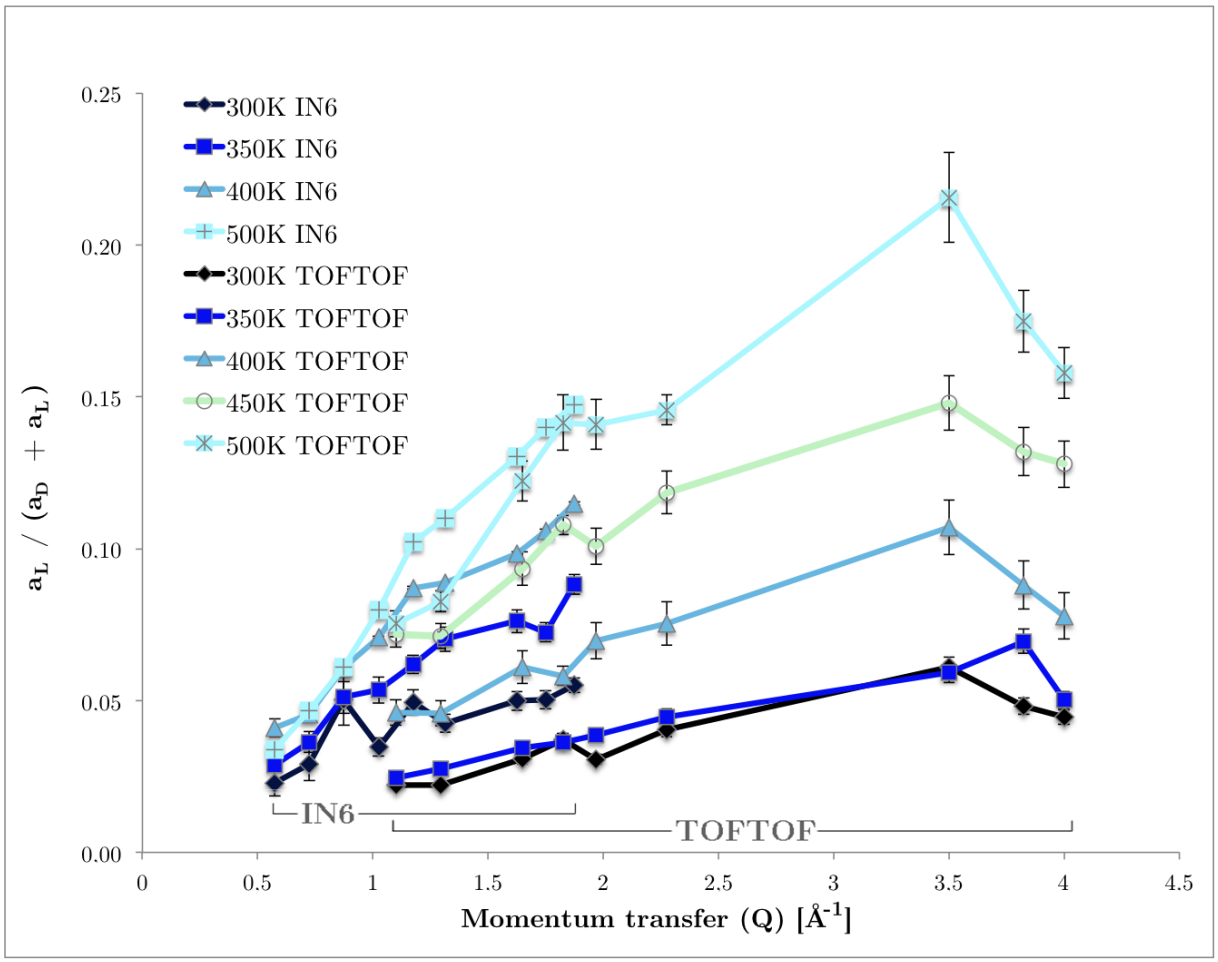

Figure 3.6: Inelastic EISF for 10Sc:BZO, comparing results from IN6 and TOFTOF instruments.

In Fig. 3.6, the EISF for 10Sc:BZO is shown over the full Q-range investigated. The figure shows data both from the IN6 instrument (traditional momentum transfer range) and from the TOFTOF instrument (extended momentum transfer range). Concerning Fig. 3.6, it must be stressed that these two experiments probe proton dynamics of different time and length scales (see again Fig. 2.2), not necessarily operating through the same local mechanisms. Thus their EISF are not expected to be the same. It is observed that the results indeed differ significantly. In the 1 <Q <2 range, where information is available for both experiments, proton dynamics are more prominent in the time- and length scales probed by IN6 than in the time and

length scales probed by TOFTOF. At 400 K and 1.5 $Å^{-1}$, for instance, roughly 10% of the total scattering relates to quasi-elastic broadening (which can predominantly be correlated to proton dynamics, as argued in the discussion concerning Table 2.1) through the time and length-scale window of IN6, while this number is only 5% when viewed through the time and length window of TOFTOF. This difference is strongly temperature dependent. At lower temperature than 400 K, the proton dynamics taking place within the distance and time window of TOFTOF are weak. In particular, the TOFTOF data shows no significant increase in dynamics from 300 K to 350 K, indicating that the dynamics probed by TOFTOF may be subject to a high onset temperature, above 350K. At the highest temperature measured (500 K) however, dynamics taking place within the time and length window of TOFTOF takes on a magnitude comparable to those visible through IN6.

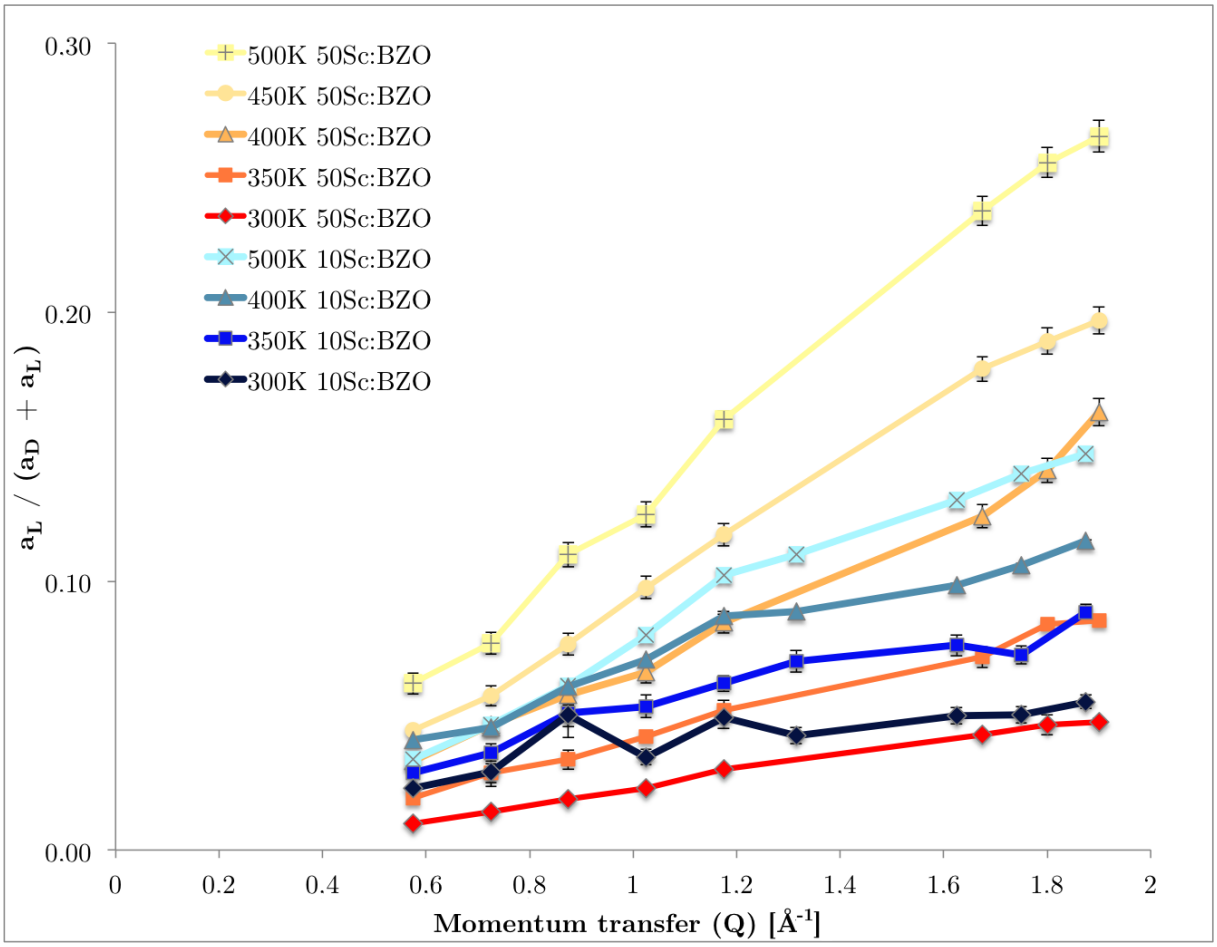

Figure 3.7: Comparison of quasielastic EISF for 10Sc:BZO and 50Sc:BZO, using data from IN6 covering a traditional momentum transfer range.

At 3.5 $Å^{-1}$, the 10Sc:BZO structure reaches a maximum of more than 20% of TOFTOF-visible scattering being due to quasi-elastic broadening. This figure is in line with previous studies [12], with the most recent study showing a figure of 25% measured with an instrument probing a similar range in time and length-scale as TOFTOF (IN5 at Institut Laue-Langevin using the same 2.5 Å wavelength as in the present work). The above-mentioned percentages cannot, however, be directly

assigned a distinct physical interpretation, such as percentage of protons being mobile, but should be interpreted as relative measure.

A comparison between the time- and length-scales of TOFTOF and IN6 experiments respectively may, in relation to Fig. 3.6, provide some hints about the microscopic dynamics. In particular, it is interesting that the TOFTOF-visible proton dynamics, probing a rapid time-scale in the low picosecond to sub-picosecond range, appear to require temperatures well above 350 K to reach significant magnitudes. The short time-scales probed are close to the first optic phonon band, typically observed around 10-15 meV in perovskites, corresponding to a period of about 0.3 ps [**?**]. The motions associated to the first optic bands involve tilting motion of the $Zr(Sc)O_6$ octahedra, which strongly affect the hydrogen bond length and may, locally, lower the potential energy barrier for proton jumps.

QENS on 50Sc:BZO was only performed at the IN6 instrument, in experimental settings directly comparable to the IN6 measurement on 10Sc:BZO. In Fig. 3.7, the EISF 50Sc:BZO is displayed together with the already-presented IN6 results on 10Sc:BZO. We note, not surprisingly, that the overall proton dynamics are significantly more prominent in 50Sc:BZO. This can be explained by the larger number of protons. More interestingly, the 50Sc:BZO exhibits a seemingly similar temperature behaviour to the IN6 measurements on 10Sc:BZO; proton dynamics grow significantly even between 300 K to 350 K.

In 50Sc:BZO, the quasi-elastic component account for 27% of total scattering intensity at 500 K and Q = 1.90 $Å^{-1}$, roughly twice as much as in 10Sc:BZO. It could be argued that this is still a small difference considering the difference in number of available protons, suggesting a higher average proton mobility in 10Sc:BZO.

3.3.2 Lorentzian FWHM and Correlation Times

A consistent Q-dependence of Γ was not found in any experiment, while for two experiments (the IN6 measurements of 10Sc:BZO and 50Sc:BZO) a weak but consistent temperature dependence was observed. An increase in Γ signifies a more rapid process, which is reasonable to expect for proton dynamics as temperature increases. The largely Q-independent Γ are typical of localized diffusion processes [6].

The Γ values of 10Sc:BZO from both IN6 and TOFTOF experiments are displayed in Fig. 3.8. The difference in Γ is related to the difference in resolution and consequently to the difference in time scales probed by the respective experiments. The resolution places a low-speed limit for the time-scale of each experiment, restricting also the Γ range according to eq. 2.11. The lower resolution of TOFTOF means that it probes more rapid time-scales (see again Fig. 2.2), consequently the Γ values are expected to be higher. The Γ values of 50Sc:BZO are seen together with those of 10Sc:BZO in Fig. 3.8.

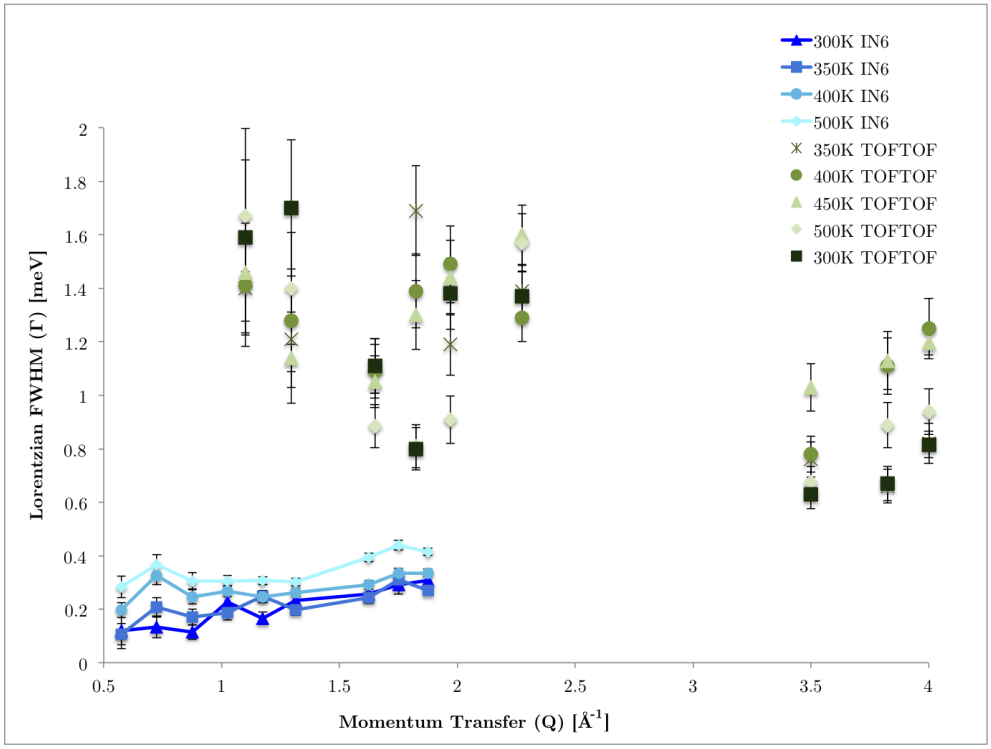

Figure 3.8: FWHM of the lorentzian contribution (Γ) for IN6 and TOFTOF measurements on 10Sc:BZO.

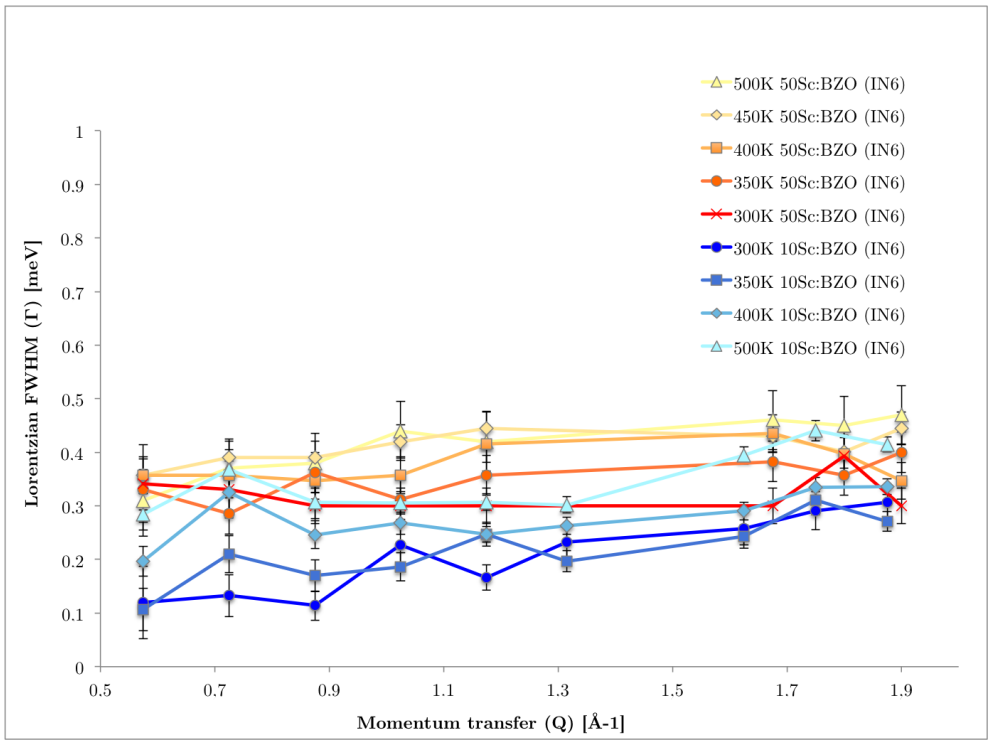

Figure 3.9: FWHM of the lorentzian contribution (Γ) for 10Sc:BZO and 50Sc:BZO, both based on IN6 data.

The temperature dependence of Γ will be further discussed in term of activation energy hereafter for the IN6 data set, but, unfortunately, no reliable temperature dependence ofΓ can be extracted from the TOFTOF data set due to the dispersion of the data points.

3.3.3 Activation Energy

Activation energies as derived from an Arrhenius form of the temperature behaviour of Γ, are displayed in Fig. 3.10. Each data point in the Arrhenius plot represents a *Q-average* of ln(Γ) values for each particular temperature. The error bars thus represents the standard deviation of each $\ln(\Gamma(Q))_T$ sample.

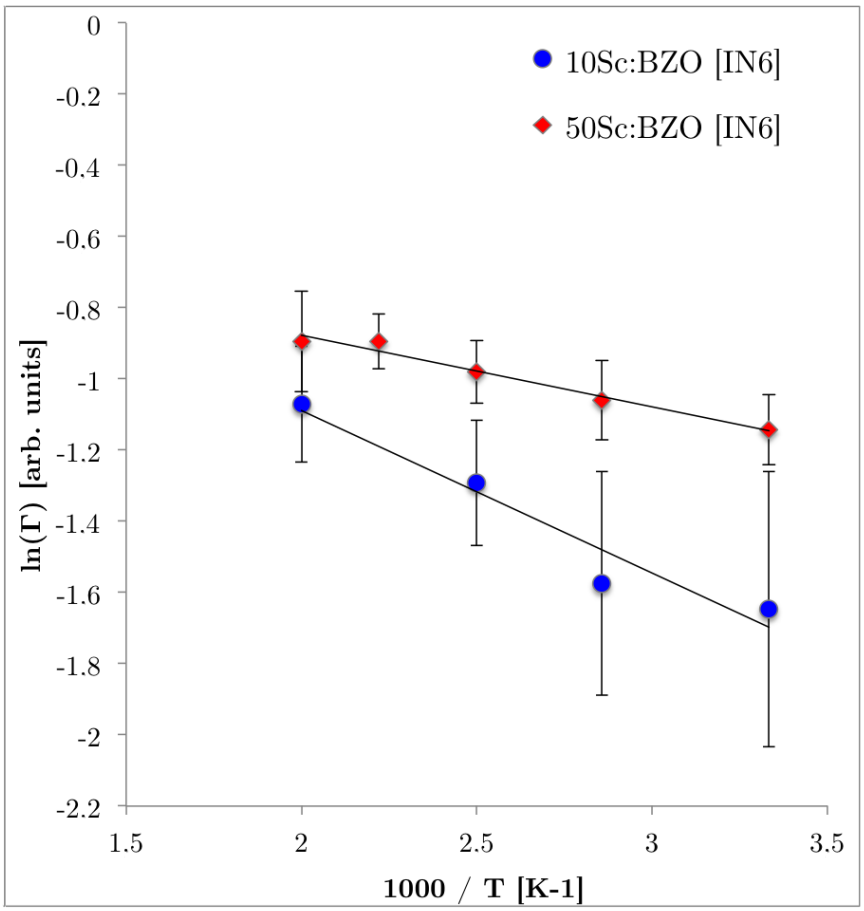

Figure 3.10: Arrhenius plot for 10Sc:BZO and 50Sc:BZO (data from IN6).

The activation energies were estimated, from the slopes of the Arrhenius plot, to be 46 meV (within 1.5 – 83 meV) for 10Sc:BZO and 20 meV (within 1 – 36 meV) for 50Sc:BZO. The error margins are based on the maximum and minimum slopes possible to fit within the error bars of the data sets. The values for 10Sc:BZO lay inbetween the results in Refs. [12] and [13].

It should be stressed that activation energies obtained in this way merely constitute a

mean over all processes involved in the dynamics probed. Efforts have been made to relate activation energies to fundamental steps such as the proton motions depicted in Fig. 1.2, e.g. in Ref. [13].

It should also be mentioned that the activation energies for the microscopic processes probed here are not the rate limiting barrier in current macroscopic samples of these perovskite compounds. While the microscopic dynamics visible in QENS are found to exhibit energy barriers in the 10 - 100 meV range, numbers which are also confirmed reasonable using first-principles methods [6, 13, 12], long-range proton conductivity is found to exhibit an overall barrier of around 500 meV [12]. The added energy barrier in macroscopic samples has been thoughts to be due, at least in part, to grain boundary effects including oxygen depletion near the boundaries.

3.3.4 Local Diffusion Mechanisms: Comparison to Models

As discussed in relation to fig. 2.4, the r parameter for the N=2 jump model is assumed here to to correspond to half of the jump length. Ref. [12] found r to be in the 0.74 to 0.80 Å range for measurements on 10Sc:BZO at extended (1 – 4 $Å^{-1}$) Q range, and Ref. [13] found r values in the 0.82 to 0.93 Å range for the same compound at traditional (0.5 – 2 $Å^{-1}$) Q range. These values are reasonable, as the oxygen-oxygen distances in barium zirconate are approximately 2.6 to 2.9 Å [12]. Given a covalent O-H bond length in the neighborhood of 1 Å, the distance between proton positions prior to and subsequent to a jump (the jump length), would correspond to a minimum of 0.6 – 0.9 Å. Angles larger than $45 degrees$ between the Sc/Zr–O bond and H-O bond (in fig. 2.4(a), an angle of $90 degrees$ is illustrated) would increase the jump distance.

Moving to the actual data of this study, we first discuss an example of the fluidity of the r parameter for N=2. In Fig. 3.11 we fit experimental data for 50Sc:BZO from IN6 (i.e. with traditional Q range) to the N=2 model described in section 2.5. In Fig. 3.11(a), the fitting is conducted through a Least Square Error optimization scheme in MATLAB for each temperature individually. The r parameter here assumes values in the 0.91˘1.08Å range. In Fig. 3.11(b) and Fig. 3.11(c), we instead fit the data using forced r parameter values of 0.80 and 1.20Å respectively. We observe that for $r = 0.80$, the fits are mostly consistent with experimental data at high Q values while deviating at the lowest Q values. With $r = 1.20$, the fits appear inconsistent with the overall shape spanned by the experimental data points, with the N=2 model curves reaching their maxima at Q values seemingly too low. This acts to show that while the fit in Fig. 3.11(a) indeed exhibit the minimum overall error, a fit using $r = 0.80$ also provides a reasonable fit. Particularly considering that the data points at lowest Q carry the highest relative uncertainties and are more prone to errors from data treatment such as background subtraction.

Fits to the other experimental data (10Sc:BZO over traditional as well as extended Q range), are shown in fig. 3.12. Here, the models are only shown fitted through the Least Square Error optimization scheme. It is readily observed that for Fig.

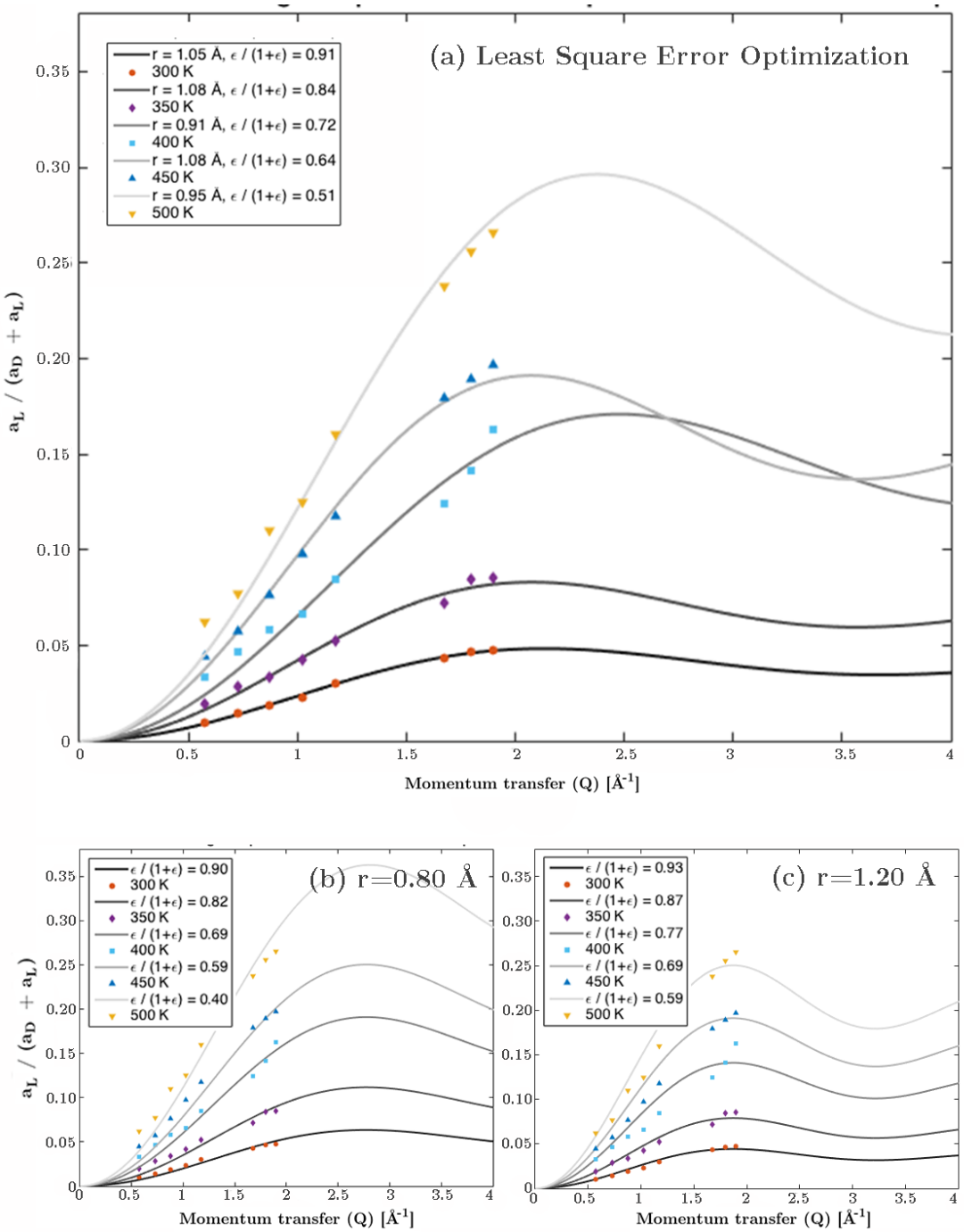

Figure 3.11: Fits of N=2 model to 50Sc:BZO experimental data from IN6 (traditional Q range). Top section displays the best-fit r and ϵ parameters, while the lower left and lower right sections displays fits using forced r parameters, using too small and too large r respectively.

3.12(a), displaying the fits in traditional Q range, the models do not achieve a reasonable fit to experimental data. In particular, the experimental data points at low Q values display an EISF ratio too large to allow for an intercept at EISF = 0 as assumed by the model. As a consequence, the maxima of the curves appear

shifted to low Q. A maximum at a Q value too low corresponds to the r parameter being overestimated. Indeed, we see that the r parameters obtained in Fig. 3.12(a) (1.14˘1.53Å) are significantly higher than in previous studies and mostly outside our range of physically reasonable values.

Table 3.1: Table over parameters obtained from best-fit models. Note that the immobile fractions ϵ are referring specifically to the ratio $\epsilon/(1+\epsilon)$.

Temperature	300 K	350 K	400 K	450 K	500K
r (*jump length*) **N=2**					
10Sc:BZO (IN6)	1.53	1.33	1.29		1.14
10Sc:BZO (TOFTOF)	0.70	0.68	0.73	0.75	0.73
50Sc:BZO (IN6)	1.04	1.05	0.94	1.03	1.04
ϵ (*immobile fraction*) **N=2**					
10Sc:BZO (IN6)	0.97	0.87	0.82		0.77
10Sc:BZO (TOFTOF)	0.91	0.90	0.84	0.76	0.68
50Sc:BZO (IN6)	0.92	0.86	0.73	0.67	0.56
r (*jump length*) **N=4**					
10Sc:BZO (IN6)	2.77	2.45	2.50		2.18
10Sc:BZO (TOFTOF)	1.25	1.22	1.29	1.33	1.30
50Sc:BZO (IN6)	2.10	2.11	1.97	2.09	2.09
ϵ (*immobile fraction*) **N=4**					
10Sc:BZO (IN6)	0.94	0.91	0.88		0.85
10Sc:BZO (TOFTOF)	0.94	0.93	0.89	0.83	0.78
50Sc:BZO (IN6)	0.95	0.91	0.84	0.80	0.73

Table 3.2: Table of model parameters from previous studies on 10Sc:BZO. Numbers marked "Karlsson" refers to results from Ref. [13], conducted on traditional (max. 2 $Å^{-1}$), numbers marked "Noferini" refers to Ref. [12], conducted on extended momentum transfer range (max. 4 $Å^{-1}$). Standard deviations reported by Karlsson are 0.06 to 0.14 $Å^{-1}$, standard deviations reported by Noferini are 0.01 to 0.02 $Å^{-1}$

Temperature (K)	300	350	380	430	450	465	495	550
r (*jump length*) **N=2**								
Karlsson (2009)			0.93	0.83		0.82	0.82	
Noferini (2017)	0.74	0.76			0.78			0.80
r (*jump length*) **N=4**								
Karlsson (2009)			1.10	0.98		0.97	0.96	
Noferini (2017)	0.92	0.96			0.99			1.02

Comparing both the N=2 (jump motion) and N=4 (O-H rotation) models, in Fig. 3.12 we show both models plotted together for IN6 (top) and TOFTOF data (bottom) of 10Sc:BZO respectively.

In the TOFTOF data (Fig. 3.12(b)), the three high-Q points appear to increase robustness. It is observed in Fig. 3.12(b) that the models show an improved overall

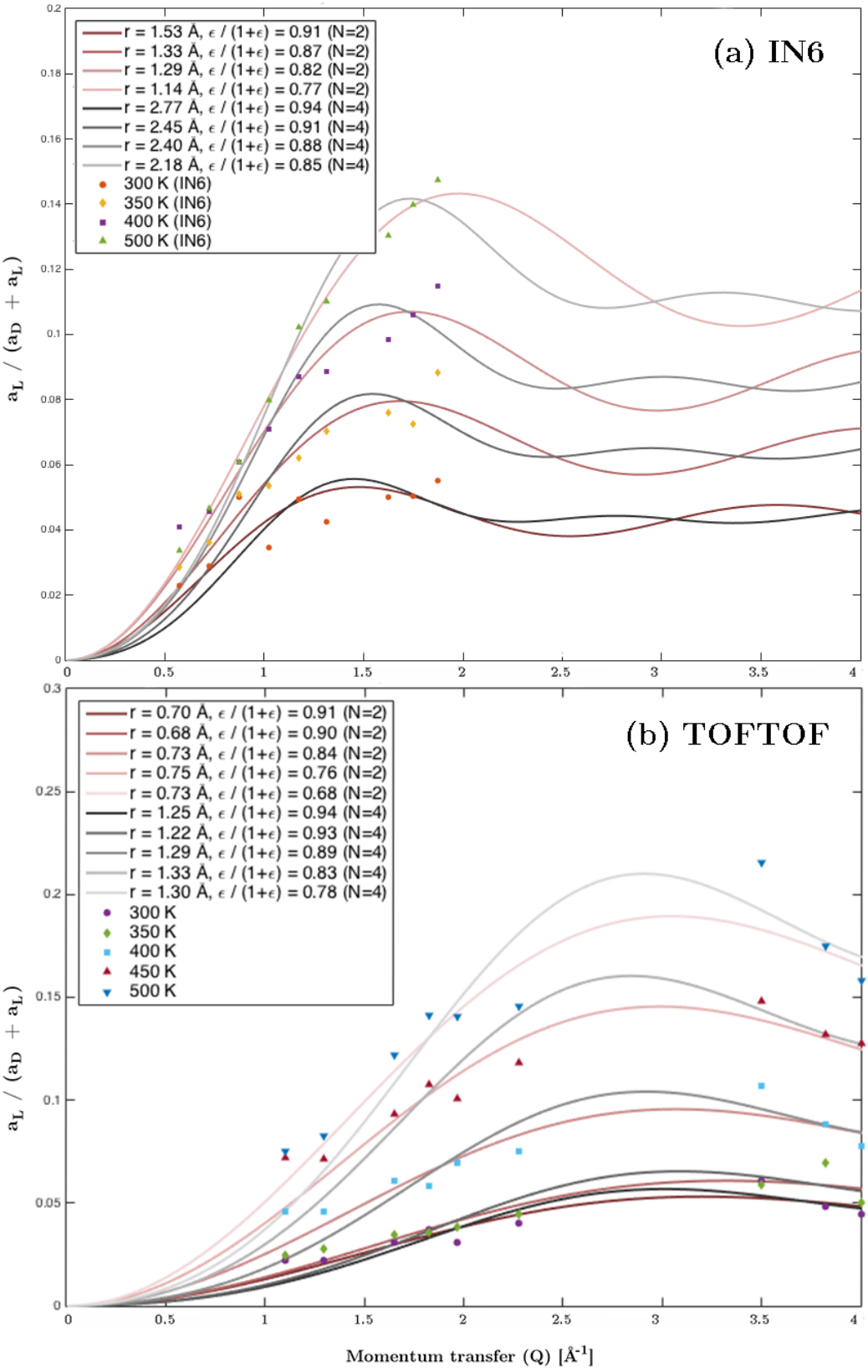

Figure 3.12: Fits of N=2 and N=4 models to 10Sc:BZO experimental data from IN6 (traditional Q range) and TOFTOF (extended Q range).

fit to the shape of experimental data. The parameters obtained for N=2 are similar to the one obtained in Ref. [12] (our fits yield $r = 0.68 - 0.75$Å, while Noferini finds 0.74˘0.80Å). Note that in Ref. [12], data points at Q values lower than about 1.5Å^{-1} do not exist. Values of all parameters are displayed in Table 3.2.

For the N=4 model, all fits show r parameters larger than previous studies. The 10Sc:BZO TOFTOF data (extended Q range) yields r=1.22 – 1.30 Å, compared to previous results of 0.92 – 1.10 Å [12, 13]. The previously found values are more consistent with the physical interpretation, as the r parameter for the N=4 model represents the distance of a O-H covalent bond which is normally 0.97 – 1.0 Å [12]. The fits based on traditional Q range also significantly overestimates r parameters of the N=4 model compared to previous results.

The quality of fits is not sufficient for drawing conclusions as to whether the N=2 or the N=4 model constitute the better overall fit.

For future studies, it is suggested that the fitting procedure (particularly those based on a traditional, limited Q range) may take additional information into account to improve reliability. Such information could include average slopes for some n-point segments or knowledge gained from the extended Q range measurements regarding the position of the EISF curve maxima. Alternatively, the consistent overestimation of lorentzian contribution at low Q in relation to models may have physical reasons such as multiple scattering having a large impact at low scattering angles. In that case, a constant allowing for to non-zero intercept should be introduced in the fitting procedure to account for this effect, provided the offset remains small in relation to the overall signal.

4

Conclusions

The difference in "onset temperature" observed when going from traditional to extended momentum transfer range *for the same sample* (see EISF comparison for 10Sc:BZO in Fig. 3.6) illustrates what the theoretical dynamical windows (Fig. 2.2) suggest: we are not looking at situations of identical dynamics.

Correlations times τ of 10Sc:BZO results from IN6 and TOFTOF respectively, show that the two experiments probe processes of non-overlapping *mean* time-scales: 3 to 12.3 picoseconds for the IN6 measurements of 10Sc:BZO and 50Sc:BZO (in agreement with previous QENS studies and general characteristics of QENS [6]) while more rapid *average* time-scales of 0.8 to 2 picoseconds for the TOFTOF measurements on 10Sc:BZO.

At the highest temperature measured (500 K), IN6 and TOFTOF measurements on 10Sc:BZO recorded comparable magnitudes of proton dynamics (again Fig. 3.6). 50Sc:BZO displayed significantly more prominent proton dynamics than 10Sc:BZO (Fig. 3.7), although not to the same factor as their relative number of protons (roughly 3.5 times as many as in 50Sc:BZO than in our over-hydrated sample of 10Sc:BZO).

The extended momentum transfer range of TOFTOF proved highly useful to increase robustness when fitting experimental data to theoretical models, although the extended Q-range measurements were not useful for deriving mean activation energies due to their wider dispersion of data points.

Only the r parameter yielded by fitting the N=2 jump model to extended Q-range experimental data was consistent with previous studies. The N=2 r parameter corresponding to fits with traditional Q-range data, as well as all N=4 r parameters (both Q-ranges) appeared to be overestimated in relation to physically reasonable values. Consequently, a determination of whether the dynamics probed were mainly composed of proton jumps or of O-H rotations could not be made.

The lack of fitting accuracy could be due to Further efforts should be aimed at improving the fitting procedure e.g. by searching a reason for the apparent existence of a non-zero intercept in the EISF ratio. If a reason would be found for this consistent error, improvements could be made to the fiting procedure to account for it.

Nevertheless, it is worth mentioning that extending the Q-range appeared to contribute to robustness of the fits. Thus several uses are identified for the extended Q range measurements in yielding further clues into the fundamental steps of the Grotthus mechanism for these materials: (i) taking advantage of lower resolution to ignore slower dynamics and highlight more rapid time-scales and (ii) provide robustness to comparisons with simulations, when comparison is based on area fractions of elastic and quasi-elastic contributions (the extended Q-range does not appear as useful for determinations based on trends in Γ values).

Supplementary Material

Download of supplementary material, including raw fits of all QENS spectra, can be made through: `https://tinyurl.com/Orstadius-Suppl-Mat`

Bibliography

[1] D Marx. Proton transfer 200 years after von grotthuss: Insights from ab initio simulations. *Chemphyschem.*, 7(9):1848–1870, 2006.

[2] Colin A. Wraight. Chance and design - proton transfer in water, channels and bioenergetic proteins. *Biochimica et Biophysica Acta – Bioenergetics*, 1757(8):886–912, 2006.

[3] Paul Heitjans and Jörg Kärger. *Diffusion in Condensed Matter: Methods, Materials, Models*. Springer (Berlin), 2005.

[4] Antony Crofts. *Lecture 12: Proton Conduction, Stoiciometry*. Lecture at UIUC (1996). Available online through URL: *https://www.life.illinois.edu/crofts/bioph354/lect12.html*.

[5] C.J.T. von Grotthuss. Sur la décomposition de l'eau et des corps qu'elle tient en dissolution à l'aide de l'électricité galvanique. *Ann. Chim. (Paris)*, 58:54–73, 1806.

[6] Maths Karlsson. Proton dynamics in oxides: insight into the mechanics of proton conduction from quasielastic neutron scattering. *Phys. Chem. Chem. Phys*, 17:26–38, 2015.

[7] Hau Lin, Fei Zhou, Chi-Ping Liua, and Vidvuds Ozoliņš. Non-grotthuss proton diffusion mechanism in tungsten oxide dihydrate from first-principles calculations. *J. Mater. Chem. A*, (2):12280–12288, 2014.

[8] K. D. Kreuer. Proton-conducting oxides. *Annu. Rev. Mater. Res.*, 33:333–359, 2003.

[9] S. P. Shafi, L. Bi, S. Boulfrad, and E. Traversa. Y and ni co-doped $bazro_3$ as a proton-conducting solid oxide fuel cell electrolyte exhibiting superior power performance. *Journal of The Electrochemical Society*, 162(14):F1498–F1503, 2015.

[10] R B Cervera, S Miyoshi, Y Oyama, Y E Elammari, T Yagi, and S. Yamaguchi. Perovskite-structured $BaScO_2(OH)$ as a novel proton conductor: Heavily hydrated phase obtained via low-temperature synthesis. *Chem. Mater.*, 25:1483–1489, 2013.

[11] M. Karlsson, A. Istaq, A. Matic, and S.G. Eriksson. Short-range structure of proton-conducting $BaM_{0.10}Zr_{0.90}O_{2.95}$ (m=y, in, sc and ga) investigated with vibrational spectroscopy. *Solid State Ionics*, 181:126–131, 2010.

[12] Daria Noferini, Michael Marek Koza, and Maths Karlsson. Localized proton motions in acceptor-doped barium zirconates. *J. Phys. Chem. C*, 121:7088–7093, 2017.

[13] M Karlsson, A Matic, D Engberg, M E Björketun, M M Koza, I Ahmed, G Wahnström, L Börjesson, and S-G Eriksson. Quasielastic neutron scattering of hydrated $BaZr_{0.90}A_{0.10}O_{2.95}$ (a = y and sc). *Solid State Ionics*, 180:22–28, 2009.

[14] B. T. M. Willis and C. J. Carlile. *Experimental Neutron Scattering.* Oxford University Press (Oxford), 2009.

[15] Daria Noferini. *Neutron scattering investgations of proton dynamics in acceptor doped barium zirconates.* **Licentiate Thesis**. Dept. of Phys., Chalmers Univ. of Tech. (Gothenburg, Sweden), 2016.

[16] R. Hempelmann. *Quasielastic Neutron Scattering and Solid State Diffusion.* Oxford University Press, 2000.

[17] F. Giannici, M. Shirpour, A. Longo, A. Martorana, R. Merkle, and J. Maier. Long-range and short-range structure of proton-conducting YY. *Chem. Mater.*, 23:2994–3002, 2011.

[18] D. Z. Sahraoui and T. Mineva. Effect of dopant nature on structures and lattice dynamics of proton-conducting $BaZrO_3$. *Solid State Ionics*, 253:195–200, 2013.

[19] M. Karlsson, A. Matic, C.S. Knee, I. Ahmed, L. Borjesson, and S.G. Eriksson. Short-range structure of proton-conducting perovskite $BaIn_xZr_{1-x}O_{3-x/2}$ (x= 0 0.75). *Chem. Mater.*, 20:3480, 2008.

[20] I. Oikawa and H. Takamura. Correlation among oxygen vacancies, protonic defects, and the acceptor dopant in sc-doped $BaZrO_3$ studied by ^{45}Sc nuclear magnetic resonance. *Chem. Mater.*, 27:6660–6667, 2015.

[21] Laura Mazzei. *Protons in In-doped $BaZrO_3$: incorporation, distribution and local environments.* **Licentiate Thesis**. Dept. of Phys., Chalmers Univ. of Tech. (Gothenburg, Sweden), 2016.